# On Magic State Distillation using Nuclear Magnetic Resonance

by

Adam Hubbard

A thesis
presented to the University of Waterloo
in fulfillment of the
thesis requirement for the degree of
Master of Science
in
Physics

Waterloo, Ontario, Canada, 2008

I hereby declare that I am the sole author of this thesis. This is a true copy of the thesis, including any required final revisions, as accepted by my examiners.

A. Hubbard

I understand that my thesis may be made electronically available to the public.

A. Hubbard

# Abstract

Physical implementations of quantum computers will inevitably be subject to errors. However, provided that the error rate is below some threshold, it is theoretically possible to build fault tolerant quantum computers that are arbitrarily reliable. A particularly attractive fault tolerant proposal, due to its high threshold value, relies on Clifford group quantum computation and access to ancilla qubits. These ancilla qubits must be prepared in a particular state termed the 'magic' state. It is possible to distill faulty magic states into pure magic states, which is of significant interest for experimental work where perfect state preparation is generally not possible.

This thesis describes a liquid state nuclear magnetic resonance based scheme for distilling magic states. Simulations are presented that indicate that such a distillation is feasible if a high level of experimental control is achieved. Preliminary experimental results are reported that outline the challenges that must be overcome to attain such precise control.

# Acknowledgements

First and foremost I would like to thank my incredible wife Kara. Her love and support are not only the foundation, but the inspiration for any of my successes.

Furthermore, I would like to thank my parents, Ken and Doris, for instilling in me a desire to learn and for continually encouraging me. I am also fortunate to have a wonderful brother and amazingly supportive in-laws.

I would also like to thank Colm Ryan and Stephanie Simmons for their help with this project and Camille Negrevergne, Josh Slater, and Nathan Babcock for their efforts laying the groundwork. Also I would like to thank Martin Laforest, Marcus Silva, and Osama Moussa, for their camaraderie and answers to random questions, and Mike Ditty for continually fixing the spectrometer.

I must thank Dr. Raymond Laflamme for the opportunities he has provided and his assistance through tough times, both professionally and personally. Furthermore, I am grateful to Dr. Gregor Weihs, Dr. Bill Power, and Dr. Jonathan Baugh for their insights and participation on my advisory and defense committees.

Finally, I am grateful to Ray, the Natural Sciences and Engineering Council of Canada, the Bell Family Fund, and the University of Waterloo for their financial support.

# Dedication

To Duane.

# Contents

# List of Tables

# List of Figures

# Chapter 1

# Introduction

Interest in computational devices that exploit quantum mechanical properties has grown significantly as scientific and technological advances have enabled increasingly precise control over quantum systems. Significant theoretical work in this area has shown that quantum information processing (QIP) devices are able to simulate quantum systems [8] and implement certain difficult computational tasks, such as factoring large numbers, without the exponential costs in time or computational resources associated with classical methods [21, 20].

In [7] DiVincenzo presents generally accepted criteria for a physical implementation of a QIP device. As any physical implementation will be subject to errors, one must be able to implement these criteria in a fault tolerant manner. One method to achieve such fault tolerance is to encode the state of single quantum bits (qubits) into blocks of several qubits that are more robust to errors. By performing encoded gates on the encoded qubits it is possible to process information. Furthermore, periodic error correction prevents the accumulation of error [18]. In these models, as long as the error rate is below a certain threshold, the computations can be made arbitrarily reliable [18]. Unfortunately, most models require an error rate threshold that is beyond current experimental abilities [14, 22, 6].

To address this, Bravyi and Kitaev have proposed a model that can achieve higher threshold values by limiting the errors that need to be corrected [5]. A requirement for

this model is that a supply of faulty 'magic' states can be purified (distilled). Therefore, in the pursuit of experimental fault tolerance it becomes significant to determine if sufficient experimental control exists to implement such a distillation.

The goal of this project is to determine whether sufficient experimental control exists in nuclear magnetic resonance (NMR) QIP to demonstrate the successful distillation of a magic state. NMR was chosen as the implementation medium due to its ability to precisely control a sufficiently large quantum system.

The following work is organized as follows. First, there is an overview of Bravyi and Kitaev's proposed computational model, including the role of magic state distillation. Following that is a brief overview of NMR and how it can be used for QIP. A variant of the magic state distillation procedure that works within the restrictions imposed by NMR QIP is then presented along with simulations that indicate that successful distillation is within reach with the current level of experimental control. Finally, preliminary experimental work towards such a distillation is summarized.

# Chapter 2

# Magic State Theory

## 2.1 Computational Model

In order to demonstrate a fault tolerant architecture with a high error rate threshold, Bravyi and Kitaev proposed a universal quantum computation model in which only certain operations are faulty, while the remaining operations are implemented ideally [5]. Particularly, Clifford group quantum computation is implemented ideally. Specifically, one has the ability to ideally:

1. Prepare qubits in the state $|0\rangle$.
2. Apply Clifford group operators to the state.
3. Perform non-destructive projective measurements of the eigenvalues of a Pauli operator.

The Pauli group is defined as $\{X, Y, Z, I\}$ where

$$X = \begin{pmatrix} 0 & 1 \\ 1 & 0 \end{pmatrix}, \quad Y = \begin{pmatrix} 0 & -i \\ i & 0 \end{pmatrix}, \quad Z = \begin{pmatrix} 1 & 0 \\ 0 & -1 \end{pmatrix}, \quad I = \begin{pmatrix} 1 & 0 \\ 0 & 1 \end{pmatrix} \tag{2.1}$$

and the Clifford group is the group of operators that map the Pauli group onto itself. It is a finite subgroup of $U(2^n)$ generated by the Hadamard, $H$, the phase-shift gate, $S$, and

the controlled-not gate, $CNOT$.

$$H = \frac{1}{\sqrt{2}}\begin{pmatrix}1 & 1\\ 1 & -1\end{pmatrix}, \quad S = \begin{pmatrix}1 & 0\\ 0 & i\end{pmatrix}, \quad CNOT = \begin{pmatrix}I & 0\\ 0 & X\end{pmatrix} \tag{2.2}$$

Clifford operators are included in the list of ideal operations because it is possible to use concatenated stabilizer codes to implement the gates fault tolerantly with arbitrarily low error rates [5]. For more information on stabilizers and error correcting codes see [18]. The model also uses adaptive computation, meaning that an operation can depend on previous measurement outcomes.

The operations listed above are not sufficient for universal quantum computing, as they can be efficiently simulated on a classical computer [11, 18]. However, universal quantum computing can be achieved by adding a fourth operation to the model.

4. Preparation of the state $\rho = \frac{1}{2}\left[I + \frac{1}{\sqrt{3}}\left(p_x X + p_y Y + p_z Z\right)\right]$.

Note that if $\frac{1}{\sqrt{3}}\left(|p_x| + |p_y| + |p_z|\right) \leq 1$ the state $\rho$ can be prepared efficiently with probabilistic Clifford group computation. For example, imagine starting in the state $|0\rangle$ and with equal probability either doing nothing, rotating the state to $(I + X)$, or rotating the state to $(I + Y)$. In this situation $p_x = p_y = p_z = 1/\sqrt{3}$. However as the total probability for these actions must sum to 1 it is impossible to use the ideal operations to prepare states with $\frac{1}{\sqrt{3}}\left(|p_x| + |p_y| + |p_z|\right) > 1$.

Bravyi and Kitaev show that if $\rho$ lies in a significant portion of the Bloch sphere [18] exterior to the octahedron formed by $\frac{1}{\sqrt{3}}\left(|p_x| + |p_y| + |p_z|\right) = 1$, it is possible to achieve universal quantum computation [5]. They define this subset of states by calculating the maximum fidelity between $\rho$ and the pure state $U|T_0\rangle\langle T_0|U^\dagger$, where $U$ is a single qubit Clifford operator and $|T_0\rangle\langle T_0|$ is a 'magic' state defined as

$$|T_0\rangle\langle T_0| = \frac{1}{2}\left[I + \frac{1}{\sqrt{3}}\left(X + Y + Z\right)\right]. \tag{2.3}$$

The maximum fidelity $F_T(\rho)$ between $\rho$ and $U|T_0\rangle$ is given by

$$F_T(\rho) = \max_{U \in \mathcal{C}_1} \sqrt{\langle T_0|U^\dagger \rho U|T_0\rangle}. \tag{2.4}$$

One is able to simulate universal quantum computation whenever

$$F_T(\rho) > F_T \equiv \left[\frac{1}{2}\left(1+\sqrt{\frac{3}{7}}\right)\right]^{\frac{1}{2}} \approx 0.910. \tag{2.5}$$

Note that states lying on or in the above mentioned octahedron consist of all states $\rho_O$ such that

$$F_T(\rho_O) \leq F_T^* \equiv \left[\frac{1}{2}\left(1+\sqrt{\frac{1}{3}}\right)\right]^{\frac{1}{2}} \approx 0.888. \tag{2.6}$$

It is not currently understood whether states with fidelities between $F_T$ and $F_T^*$ would enable universal quantum computation.

## 2.2 Using Magic States to Enable Universal Quantum Computation

As stated above, universal quantum computation is possible if one has access to the ideal operations and a supply of faulty magic states [5]. First it is shown how pure magic states enable universal quantum computation and then in section 2.3 it is demonstrated how faulty magic states can be distilled to pure magic states.

The following procedure uses magic state ancillas to enable universal quantum computation. This procedure can be split into two general steps.

Step 1 - Prepare the state

$$|A_{-\pi/6}\rangle = \frac{1}{\sqrt{2}}\left(|0\rangle + e^{-i\frac{\pi}{6}}|1\rangle\right). \tag{2.7}$$

a. Prepare $|T_0\rangle \otimes |T_0\rangle$ where

$$|T_0\rangle = \cos\left(\frac{\alpha}{2}\right)|0\rangle + e^{i\frac{\pi}{4}}\sin\left(\frac{\alpha}{2}\right)|1\rangle \tag{2.8}$$

where $\alpha = \arccos\frac{1}{\sqrt{3}}$. Therefore

$$\begin{aligned}|T_0\rangle \otimes |T_0\rangle = \cos^2\left(\frac{\alpha}{2}\right)|00\rangle + e^{i\frac{\pi}{4}}\cos\left(\frac{\alpha}{2}\right)\sin\left(\frac{\alpha}{2}\right)|01\rangle \\ + e^{i\frac{\pi}{4}}\cos\left(\frac{\alpha}{2}\right)\sin\left(\frac{\alpha}{2}\right)|10\rangle + e^{i\frac{\pi}{2}}\sin^2\left(\frac{\alpha}{2}\right)|11\rangle.\end{aligned} \tag{2.9}$$

b. Measure the stabilizer $ZZ$ and discard the state if the outcome is '-1'. If the outcome is '+1' the state becomes (after a renormalization of $\sqrt{\frac{2}{3}}$)

$$|\psi_1\rangle = \cos\gamma|00\rangle + i\sin\gamma|11\rangle \tag{2.10}$$

with $\gamma = \frac{\pi}{12}$. This outcome occurs with probability

$$\cos^4\left(\frac{\alpha}{2}\right) + \sin^4\left(\frac{\alpha}{2}\right) = \frac{2}{3}. \tag{2.11}$$

Therefore one third of the time this process will fail and need to be repeated, consuming more $|T_0\rangle$ states. On average 3 states are required for each success.

c. Apply a CNOT gate controlled on the first qubit then discard the second qubit. The state becomes

$$|\psi_2\rangle = \left(\cos\gamma|0\rangle + i\sin\gamma|1\rangle\right). \tag{2.12}$$

d. Apply a Hadamard gate

$$\begin{aligned} |\psi_3\rangle &= \frac{1}{\sqrt{2}}\left\{\cos\gamma\left(|0\rangle + |1\rangle\right) + i\sin\gamma\left(|0\rangle - |1\rangle\right)\right\} &(2.13)\\ &= e^{i\gamma}\left(|0\rangle + e^{-i2\gamma}|1\rangle\right) = |A_{-\pi/6}\rangle. &(2.14)\end{aligned}$$

Step 2 - Use the state $|A_{-\pi/6}\rangle$ to implement a phase shift gate $S(e^{-i\pi/6})$ on the state $|\psi_0\rangle = a|0\rangle + b|1\rangle$ where

$$S(e^{-i\pi/6}) = \begin{pmatrix} 1 & 0 \\ 0 & e^{-i\pi/6} \end{pmatrix}. \tag{2.15}$$

a. Prepare the state $|\psi_0\rangle \otimes |A_{-\pi/6}\rangle$

$$|\psi_0\rangle \otimes |A_{-\pi/6}\rangle = \frac{1}{\sqrt{2}}\left(a|00\rangle + ae^{-i\pi/6}|01\rangle + b|10\rangle + be^{-i\pi/6}|11\rangle\right). \tag{2.16}$$

b. Measure the stabilizer $ZZ$.

i. If the outcome is '+1' then the state becomes

$$|\psi_1^+\rangle = \frac{1}{\sqrt{2}}\left(a|00\rangle + be^{-i\pi/6}|11\rangle\right). \tag{2.17}$$

ii. If the outcome is '-1' then the state becomes

$$|\psi_1^-\rangle = \frac{1}{\sqrt{2}}\left(ae^{-i\pi/6}|01\rangle + b|10\rangle\right). \tag{2.18}$$

c. Apply CNOT controlled by the first qubit.

$$|\psi_2^+\rangle = \frac{1}{\sqrt{2}}\left(a|0\rangle + be^{-i\pi/6}|1\rangle\right)|0\rangle \tag{2.19}$$

$$|\psi_2^-\rangle = \frac{1}{\sqrt{2}}\left(ae^{-i\pi/6}|0\rangle + b|1\rangle\right)|1\rangle \tag{2.20}$$

Depending on the known eigenvalue of the second qubit

$$|\psi_3\rangle = \frac{1}{\sqrt{2}}\left(a|0\rangle + be^{\mp i\pi/6}|1\rangle\right) \tag{2.21}$$

$$= S(e^{\mp i\pi/6})|\psi_0\rangle \tag{2.22}$$

where the sign of the phase is chosen randomly but is known.

Applying the process a certain number of times applies the unitary $S(e^{-ni\pi/6})$ where $n$ is an integer obeying random walk statistics. Sooner or later $n = 1$ and the desired transformation is applied. Note that because $\frac{\pi}{6}$ is a rational multiple of $2\pi$ the probability that more than $N$ steps is needed decreases exponentially with $N$ [5].

The phase shift gate $S(e^{-i\pi/6})$, together with the Clifford operators, forms a universal set of gates [23, 5].

## 2.3 Distillation of Magic States

A brief theoretical outline of the magic state distillation procedure is given below. For a complete derivation of the process see [5].

In general, the distillation algorithm transforms five copies of a faulty magic state given by

$$|T^{enc}\rangle\langle T^{enc}| \quad = \quad ((1-\epsilon)|T_0\rangle\langle T_0| + \epsilon|T_1\rangle\langle T_1|)^{\otimes 5} \tag{2.23}$$

where

$$\epsilon = 1 - \langle T_0|\rho|T_0\rangle \tag{2.24}$$

and $|T_1\rangle\langle T_1| = \frac{1}{2}[I - \frac{1}{\sqrt{3}}(X+Y+Z)]$ into a single magic state having a smaller error probability, $\epsilon$. If one defines the purity of the state as $p_{avg} = \frac{1}{3}(p_x + p_y + p_z)$, then

$$|T^{enc}\rangle\langle T^{enc}| \quad = \quad \left(\frac{1}{2}\left[I + \frac{p_{avg}}{\sqrt{3}}(X+Y+Z)\right]\right)^{\otimes 5}. \tag{2.25}$$

A faulty magic state of the form in equation 2.25 can be created from a general faulty state, $\rho = \frac{1}{2}\left[I + \frac{1}{\sqrt{3}}(p_x X + p_y Y + p_z Z)\right]$, by performing the dephasing transformation $D(\rho) = \frac{1}{3}(\rho + T\rho T^\dagger + T^\dagger \rho T)$ where

$$T = e^{i\frac{\pi}{4}}SH = \frac{e^{i\frac{\pi}{4}}}{\sqrt{2}}\begin{pmatrix} 1 & 1 \\ i & -i \end{pmatrix} \tag{2.26}$$

and $TXT^\dagger = Z$, $TYT^\dagger = X$, $TZT^\dagger = Y$.

Specifically the distillation algorithm involves measurement of the stabilizers $S_1$, $S_2$, $S_3$, $S_4$ where

$$S_1 = XZZXI \tag{2.27}$$

$$S_2 = IXZZX \tag{2.28}$$

$$S_3 = XIXZZ \tag{2.29}$$

$$S_4 = ZXIXZ \tag{2.30}$$

$$S_5 = S_1 S_2 S_3 S_4. \tag{2.31}$$

If the measurement outcome for any of these stabilizer is '-1' the distillation fails and the state is discarded. If all of the stabilizer measurement outcomes are '+1', corresponding to

the trivial syndrome, the distillation is successful. Application of a decoding transformation takes the reduced state to a single qubit state, the output of the algorithm. The entire process can be iteratively repeated using five output states as the input states for the next round of distillation.

Let $P_S$ be the orthogonal projector onto the two-dimensional subspace specified by $S_j|\Psi\rangle = |\Psi\rangle$. It is defined as

$$P_S = \frac{1}{16}\prod_{j=1}^{4}(I + S_j). \tag{2.32}$$

The reduced state corresponding to the trivial syndrome measurement is

$$\begin{aligned} \rho_0^{enc} &= P_S|T^{enc}\rangle\langle T^{enc}|P_S & (2.33)\\ &= \left[\frac{\epsilon^5 + 5\epsilon^2(1-\epsilon)^3}{6}\right]|T_0^{enc}\rangle\langle T_0^{enc}| + \left[\frac{(1-\epsilon)^5 + 5\epsilon^3(1-\epsilon)^2}{6}\right]|T_1^{enc}\rangle\langle T_1^{enc}| & (2.34)\end{aligned}$$

where $|T_{0,1}^{enc}\rangle\langle T_{0,1}^{enc}| = \frac{1}{2}[I \pm \frac{1}{\sqrt{3}}(X^{\otimes 5} + Y^{\otimes 5} + Z^{\otimes 5})]$. The probability for the trivial syndrome to be observed is given by

$$\begin{aligned} \theta_0 &= Tr(\rho_0^{enc}) & (2.35)\\ &= \frac{\epsilon^5 + 5\epsilon^2(1-\epsilon)^3 + (1-\epsilon)^5 + 5\epsilon^3(1-\epsilon)^2}{6}. & (2.36)\end{aligned}$$

The decoding sequence from the 5-qubit error correcting code, $U_{decode}$, maps $S_j$ for $j = 2, 3, 4, 5$ to $Z_j$ and the logical operators $X^{\otimes 5}$, $Y^{\otimes 5}$, $Z^{\otimes 5}$ to $X$,$Y$,$Z$ acting on the first qubit [3, 16]. Therefore

$$U_{decode}|T_{0,1}^{enc}\rangle = |T_{0,1}\rangle \otimes |0000\rangle. \tag{2.37}$$

After swapping the states $|T_0\rangle$ and $|T_1\rangle$ (as for small $\epsilon$ the state $\rho_{0000}$ is close to $|T_1^{enc}\rangle$ not $|T_0^{enc}\rangle$) the output state is given by

$$\rho_{out} = (1 - \epsilon_{out})|T_0\rangle\langle T_0| + \epsilon_{out}|T_1\rangle\langle T_1| \tag{2.38}$$

where

$$\epsilon_{out} = \frac{t^5 + 5t^2}{1 + 5t^2 + 5t^3 + t^5} \tag{2.39}$$

and $t = \frac{\epsilon}{1-\epsilon}$. See Figure 2.1 for a plot of $\epsilon_{out}$ versus $\epsilon$ and for a plot of $p_{out}$ versus $p_{avg}$.

If we iterate the distillation process, starting with $\epsilon > \frac{1}{2}(1 - \sqrt{\frac{3}{7}})$, the distillation procedure asymptotically creates the pure magic state while for $\epsilon < \frac{1}{2}(1 - \sqrt{\frac{3}{7}})$ the procedure produces the completely mixed state.

As the decoding is just a basis transformation from one stabilizer subspace to another, it does not matter whether the projection onto the stabilizer subspace is done before or after the decoding. This property is exploited in the NMR implementation as the application of the decoding sequence occurs prior to the measurement of the appropriate stabilizers.

Furthermore, faulty magic states do not need to be perfectly distilled to be useful - a small error rate is acceptable. In [5] Bravyi and Kitaev show that an error rate of

$$\epsilon \sim \frac{1}{L \log L} \tag{2.40}$$

provides reliable quantum computation, where $L$ is the number of non-Clifford gates in the circuit. This error rate can be achieved through distillation with resources scaling as polynomial in $\log L$.

It is because of their surprising ability to enable universal quantum computing with Clifford gates as well as the ability to be distilled by Clifford gates that these states are called magic states.

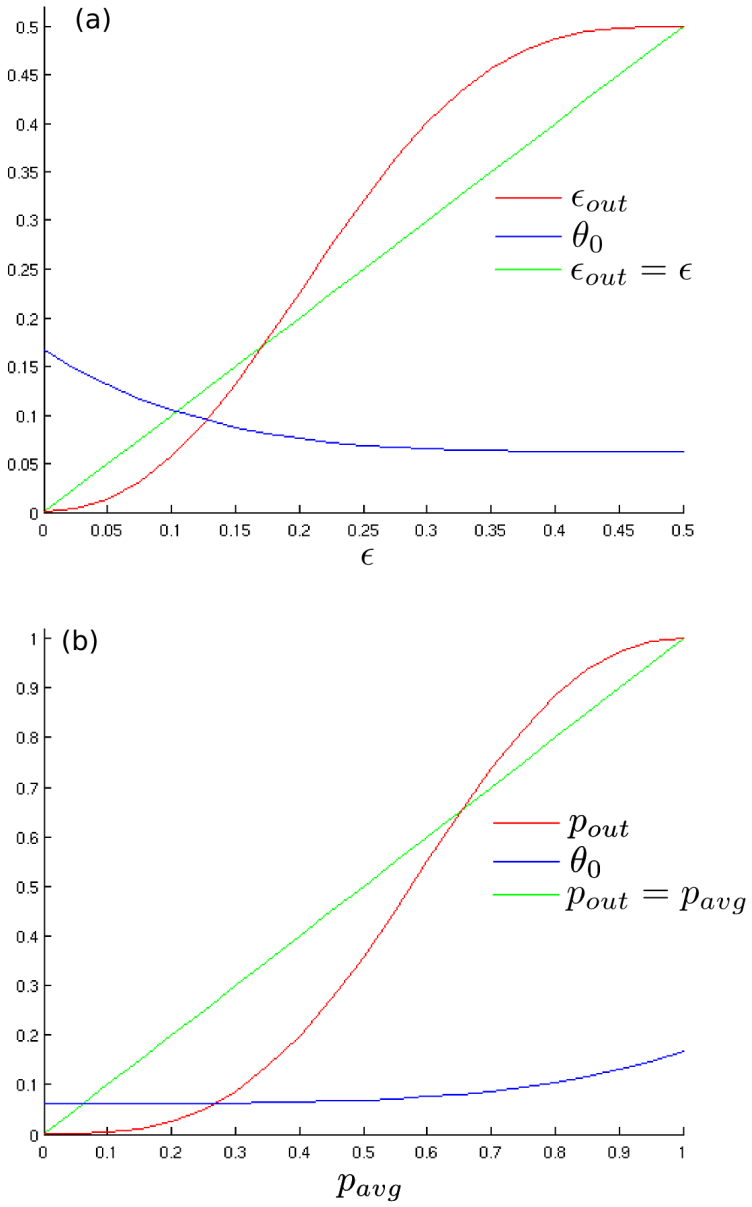


Figure 2.1: (a) The distilled error probability $\epsilon_{out}$ and the probability $\theta_0$ to measure the syndrome 0000 as a function of the initial error probability $\epsilon$. (b) The distilled purity $p_{out}$ and the probability $\theta_0$ to measure the syndrome 0000 as a function of the initial purity $p_{avg}$.

# Chapter 3

# Nuclear Magnetic Resonance

The state of a quantum mechanical spin system can be described by the density matrix $\rho(t)$, and its equation of motion given by the Liouville-von Neuman equation

$$\dot{\rho(t)} = -i[H, \rho(t)] \tag{3.1}$$

where, for time independent Hamiltonians, the solution is given by

$$\rho(t) = e^{-iHt}\rho_0 e^{+iHt}. \tag{3.2}$$

For a spin-$\frac{1}{2}$ particle the density matrix can be expanded in terms of the Pauli matrices

$$\rho = \frac{1}{2}(I + \alpha_x X + \alpha_y Y + \alpha_Z Z) \tag{3.3}$$

where $X$, $Y$, and $Z$ are the Pauli matrices and the coefficients $(\alpha_x, \alpha_y, \alpha_z)$ form the state vector on the Bloch sphere. Therefore, if the initial state, $\rho_0$, and system Hamiltonian are known, it is possible to predict the evolution of the system.

## 3.1 Hamiltonian

Classically, the energy of a magnetic moment, $\mu$, in an applied magnetic field, $\vec{B_0}$, is given by

$$E_{mag} = -\vec{\mu} \cdot \vec{B_0}. \tag{3.4}$$

A particle's intrinsic spin creates a proportional magnetic moment $\vec{\mu} = \gamma \hat{S}$ where $\hat{S}$ is the spin operator and $\gamma$ is the particle's gyromagnetic ratio [17]. Therefore for a single spin-$\frac{1}{2}$ particle in an external magnetic field, $B_0$, in the z-direction, the Hamiltonian is

$$H_Z = -\gamma B_0 \frac{Z}{2} = \omega_0 \frac{Z}{2} = \begin{pmatrix} \omega_0/2 & 0 \\ 0 & -\omega_0/2 \end{pmatrix} \tag{3.5}$$

where $\omega_0 = -\gamma B_0$ is the Larmor frequency. Consequently the spin-$\frac{1}{2}$ particle has two eigenstates of angular momentum along the z-axis termed spin up, $|0\rangle$, and spin down, $|1\rangle$, with a difference in energy between these two states of $\omega_0$. The effect of a Hamiltonian of this form is to rotate the spin about the z-axis by an angle $\omega_0 t$ in a time $t$ [17]. This rotation at the Larmor frequency is called precession.

### Radio-Frequency Pulse

Control of the spin system is accomplished by applying an oscillating magnetic field along the x-axis, while maintaining the original magnetic field in the z direction. The oscillating magnetic field along the x-axis can be decomposed as a sum of two rotating fields, the resonant, $\vec{B}^{RF}_{res}(t)$, and non-resonant, $\vec{B}^{RF}_{non-res}(t)$, components [17] where

$$\vec{B}^{RF}_{res}(t) = \frac{1}{2} B_{RF} \left\{ \cos\left(\omega_{rf} t + \phi_p\right) \hat{x} + \sin\left(\omega_{rf} t + \phi_p\right) \hat{y} \right\} \tag{3.6}$$

$$\vec{B}^{RF}_{non-res}(t) = \frac{1}{2} B_{RF} \left\{ \cos\left(\omega_{rf} t + \phi_p\right) \hat{x} - \sin\left(\omega_{rf} t + \phi_p\right) \hat{y} \right\}. \tag{3.7}$$

As it is far from resonance, the non-resonant component has almost no effect on the motion of the spins. Therefore, the Hamiltonian for the RF pulse is given by [23]

$$H_{RF} = \omega_{nut} \left\{ \cos\left(\omega_{rf} t + \phi_p\right) \frac{X}{2} + \sin\left(\omega_{rf} t + \phi_p\right) \frac{Y}{2} \right\} \tag{3.8}$$

where $\omega_{nut} = |-\frac{1}{2}\gamma B_{RF}|$ and $\phi_p$ is the phase offset.

### Rotating Frame

The description of the spin evolution can be simplified by considering the system in a frame that rotates about the z-axis at the same frequency as the radio-frequency pulse. It is shown in [17] that for such a frame the resonant RF magnetic field is stationary and the Hamiltonian becomes

$$H^{rot} = \frac{1}{2}\left[(\omega_0 - \omega_{RF})Z + \omega_{nut}(\cos\phi_p\, X + \sin\phi_p\, Y)\right]. \tag{3.9}$$

Henceforth the superscript will be dropped as the rotating frame will be considered the default frame. The evolution of a state under the above Hamiltonian is a rotation about the vector $\hat{n} = (\omega_0 - \omega_{RF})\hat{z} + \omega_{nut}(\cos\phi_p\,\hat{x} + \sin\phi_p\,\hat{y})$ as depicted in Figure 3.1.

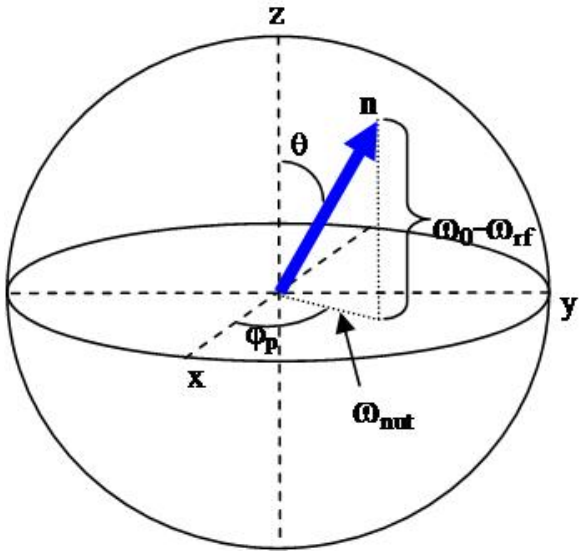


Figure 3.1: The axis of rotation for a spin state during a radio-frequency pulse as given in equation 3.9. Note that $\theta = \arctan\left(\frac{\omega_{nut}}{\omega_0 - \omega_{RF}}\right)$ and that if $\omega_0 = \omega_{RF}$ the rotation will be about the direction of $B_{RF}$, which is in the xy-plane.

### Extension to Multiple Spins

In addition to the external applied fields, the nuclei experience magnetic and electric fields which originate from other nuclei and the surrounding electrons in the sample. These interactions are grouped into the internal Hamiltonian. There are several interactions that may contribute to the internal Hamiltonian [17].

1. Chemical Shift - Shift in the Larmor frequency due to the partial shielding of the external magnetic field by surrounding electrons [23].

2. J-Coupling - Indirect magnetic interaction between nuclear spins through the electron bonds.

3. Direct Dipole-Dipole Couplings - Direct magnetic interaction of nuclear spins with each other.

4. Quadrupole Couplings - Electric interactions of spins greater than $\frac{1}{2}$ with the local electric field gradient.

5. Spin-Rotation Interaction - Magnetic interaction generated by the rotational motion of molecules.

In the case of isotropic liquids (liquids in which the translational and rotational mobilities of the molecules are the same in all directions), the internal Hamiltonian is simplified significantly. Due to the rapid motion of molecules, the direct dipole-dipole and spin-rotation interactions average to zero. Furthermore for spin-$\frac{1}{2}$ nuclei there are no quadrupole couplings, meaning that the internal Hamiltonian contains only chemical shift and J-coupling terms.

### Chemical Shift

As surrounding electrons partially shield the external magnetic field, nuclei with different chemical environments have different chemically shifted Larmor frequencies. In isotropic liquids the chemical shift is modeled by including a chemical shift term, $\delta$, in the Larmor frequency. Therefore, the chemically shifted Larmor frequency for the $i^{th}$ spin is given by

$$\omega_0^i = -\gamma\beta_0(1+\delta^i). \tag{3.10}$$

This property allows one to individually control and observe nuclei of the same species, but at different molecular locations, by slightly changing the frequency of the control fields or observation.

### J-Coupling

As the energy of two spins is lower if they are antiparallel, electrons near a nucleus tend to be polarized in the opposite sense as the nucleus, whereas distant electrons tend to be polarized in the same direction [17]. This tendency creates a coupling interaction between nuclei termed J-coupling, which is strictly intramolecular. The Hamiltonian for J-coupling is given by

$$H_J = \sum_{i<j} \frac{\pi}{2} J_{ij} \left( X^i X^j + Y^i Y^j + Z^i Z^j \right) \tag{3.11}$$

where $J_{ij}$ is the coupling strength between spins $i$ and $j$. The coupling strength depends on the nuclear species involved and decreases as the number of bonds separating the two nuclei increases [17]. If $|\omega_i - \omega_j| >> 2\pi|J_{ij}|$, which is reasonable for heteronuclear spins and small homonuclear molecules, then the above equation simplifies to [23]

$$H_J = \sum_{i<j} \frac{\pi}{2} J_{ij} Z^i Z^j. \tag{3.12}$$

Therefore, for a multiple spin system in liquid state NMR, the total Hamiltonian is the sum of the Hamiltonians due to the external $B_0$ field, the intramolecular couplings, and the applied radio frequency control fields.

## 3.2 Initial Spin State

As the energy difference between the spin up and spin down states is very small compared to the thermal energy available at room temperature, the initial system state is nearly

random. The equilibrium state for systems with small coupling, $H \approx \sum_{i=1}^{n} \omega^i \frac{Z^i}{2}$, is

$$\rho_{thermal} \approx \frac{1}{2^n} e^{-\frac{H}{kT}} \tag{3.13}$$

$$\approx \frac{1}{2^n} e^{-\frac{\omega^1}{2kT} Z^1} e^{-\frac{\omega^2}{2kT} Z^2} ... e^{-\frac{\omega^n}{2kT} Z^n} \tag{3.14}$$

$$\approx \frac{1}{2^n} \left( I^{\otimes n} - \frac{\omega^1 Z^1}{2kT} - \frac{\omega^2 Z^2}{2kT} - ... - \frac{\omega^n Z^n}{2kT} \right). \tag{3.15}$$

Therefore the initial state can be seen as the completely mixed state plus a deviation matrix

$$\rho_{thermal} = I + \sum_{i=1}^{n} \epsilon_i Z_i. \tag{3.16}$$

Although this is not the standard initial state for QIP it is possible to begin with this state for several reasons [15, 7].

1. Only the traceless part of the density matrix contributes to an observable signal.
2. All unitary and non-unitary operations used preserve the completely mixed state.
3. The size of the deviation matrix does not matter as the measurement process typically compares the relative signal strengths of some initial state to the final state. However, the deviation matrix does have to be large enough to allow magnetization detection above the noise.

In principle it is possible to use algorithmic cooling to transform the highly mixed state into a pure state, however the number of ancilla spins needed for such an operation at room temperature is impractically large ($\approx 10^{12}$) [2, 19]. In practice a pseudo-pure state is used despite the non-scalability of the preparation method [4].

## 3.3 Measurement

In order for NMR to be a viable tool for QIP it must be possible to measure the final state of the system after manipulation. This is accomplished by measuring the transverse

magnetization of the precessing spins. The macroscopic magnetization can be given as

$$\begin{aligned} M_y &= -M_0 \cos(\omega_0 t) e^{-\frac{t}{T_2^*}} \\ M_x &= M_0 \sin(\omega_0 t) e^{-\frac{t}{T_2^*}} \end{aligned}$$

where $T_2^*$ is the transverse relaxation time constant. The transverse magnetization decays because exact synchrony between the spins is lost due to small inhomogeneities in the magnetic field and intrinsic relaxation processes due to molecular motion. By placing a wire coil nearby, the precessing magnetization induces an oscillating electromotive force in the wire that can be measured.

In most situations the interaction of each nuclear spin with the coil is very weak and consequently the effect of the coil on the quantum states is negligible. By measuring the amplitude and phase of the signal, information can be gained about the state of the spin system. A more detailed discussion of NMR QIP measurement can be found in [23] and [15].

# Chapter 4

# Using NMR for QIP

Quantum computation relies on the implementation of unitary transformations on quantum states. It is a theorem of quantum information science that any unitary transformation can be composed of two-qubit CNOT gates and single qubit rotations [23]. The following demonstrates how single qubit rotations and CNOT gates are implemented in NMR QIP.

## 4.1 Single Qubit Gates

Any unitary transformation on a single quantum spin state can be viewed as a single rotation about an axis in the Bloch sphere. However, experimental control is simplified by exploiting Bloch's theorem [23], which states that for any single-qubit $U$, there exists real numbers $\alpha, \beta, \gamma$, and $\delta$ such that

$$U = e^{i\alpha} e^{-\frac{1}{2}i\beta X} e^{-\frac{1}{2}i\gamma Y} e^{-\frac{1}{2}i\delta X}. \tag{4.1}$$

This means that any arbitrary rotation, and consequently any single qubit gate, can be decomposed into rotations about the x- and y-axis. As stated earlier, when a controlled RF pulse is applied, the Hamiltonian of a single spin is

$$H = \frac{1}{2}\left((\omega_0 - \omega_{RF})Z + \omega_{nut}\left(\cos\phi_p X + \sin\phi_p Y\right)\right). \tag{4.2}$$

If $\omega_0 - \omega_{RF} = 0$ then the unitary evolution of the system is given by

$$U = e^{-i\frac{1}{2}\omega_{nut}\tau_p(\cos\phi_p X + \sin\phi_p Y)} \tag{4.3}$$

where $\tau_p$ is the pulse duration. Therefore, $U$ describes a rotation by an angle $\omega_{nut}\tau_p$ about an axis in the xy-plane given by $\cos\phi_p\,\hat{x} + \sin\phi_p\,\hat{y}$. To rotate about the x-axis one uses the phase $\phi_p = 0$, and for rotations about the y-axis one uses the phase $\phi_p = \frac{\pi}{2}$. Therefore all one needs to do to implement $X$ and $Y$ rotations (and by extension through equation 4.1 any single qubit gate) is to control the strength, duration, and phase of radio-frequency pulses at the frequency of the rotating frame.

## 4.2 CNOT Gates

The CNOT gate is implemented by using the natural J-coupling evolution of a spin system in addition to radio-frequency pulses. Using equation 3.12, the J-coupling evolution operator is given by

$$U_J(t) = e^{-i\frac{\pi}{2}J_{jk}Z^jZ^kt}. \tag{4.4}$$

Performing the following pulse sequence [23] implements the CNOT gate, up to a global phase.

$$\begin{aligned} U &= R_z^1(\frac{\pi}{2})R_z^2(-\frac{\pi}{2})R_x^2(\frac{\pi}{2})U_J(\frac{1}{2J})R_y^2(\frac{\pi}{2}) \\ &= \sqrt{-i}\begin{pmatrix} 1 & 0 & 0 & 0 \\ 0 & 1 & 0 & 0 \\ 0 & 0 & 0 & 1 \\ 0 & 0 & 1 & 0 \end{pmatrix} \end{aligned} \tag{4.5}$$

The above pulse sequences can be understood geometrically by considering the core sequence $R_x^2(\frac{\pi}{2})U_J(\frac{1}{2J})R_y^2(\frac{\pi}{2})$ [23]. This sequence applies a rotation by $\frac{\pi}{2}$ about the y-axis to qubit 2, a J-coupling evolution for $\frac{1}{2J}$s, and a rotation of the second qubit by $\frac{\pi}{2}$ about the x-axis. During the J-coupling evolution, the precession of the second spin is changed

by $\pm\frac{J_{12}}{2}$Hz, depending on whether the first spin is in the state $|1\rangle$ or $|0\rangle$. Therefore, after a delay of $\frac{1}{2J}$s, spin 2 is either at +y if spin 1 is $|0\rangle$ or at -y if spin 1 is $|1\rangle$. A final rotation about the x-axis puts spin 2 back to +z if spin 1 is $|0\rangle$ and -z if spin 1 is $|1\rangle$. The additional gates in equation 4.5 are required so that the operation works correctly on all input states. As long as two spins are connected through a network of coupled spins, it is possible to implement CNOT gates between them by moving the spin states next to each other with SWAP gates (three alternating CNOT gates) and then performing the CNOT operation.

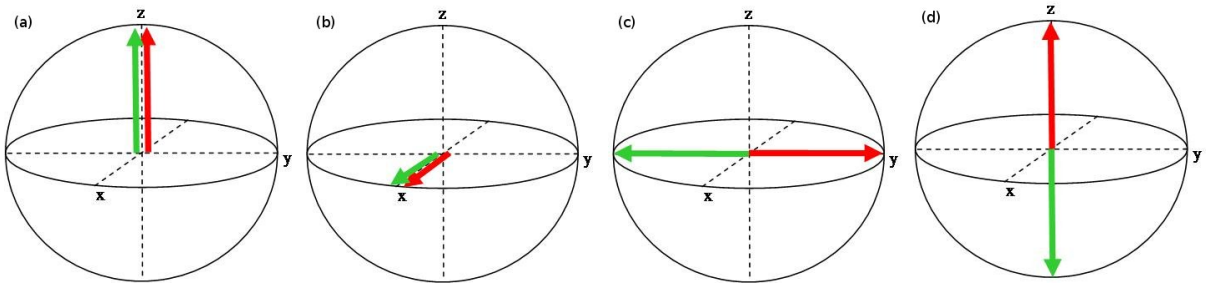


Figure 4.1: Bloch sphere representation of the target qubit during a CNOT operation. A red qubit corresponds to the control qubit being in state $|0\rangle$ while a green qubit corresponds to the control qubit being in state $|1\rangle$. The target qubit a) starts in $|0\rangle$, b) is then rotated about the y-axis, c) evolves under J-coupling, before d) being rotated about the x-axis.

## 4.3 Turning Off J-Coupling

Although it is impossible to turn the J-couplings off, it is possible to control the spins so as to cancel the effect of the J-coupling interaction over a given time period. This technique is called refocusing and involves applying a 180° pulse to one of the two coupled spins halfway through the evolution period [15]. See Figure 4.2. Refocusing can be applied efficiently to systems with more than 2 qubits, allowing one to select which qubits are effectively coupled [23].

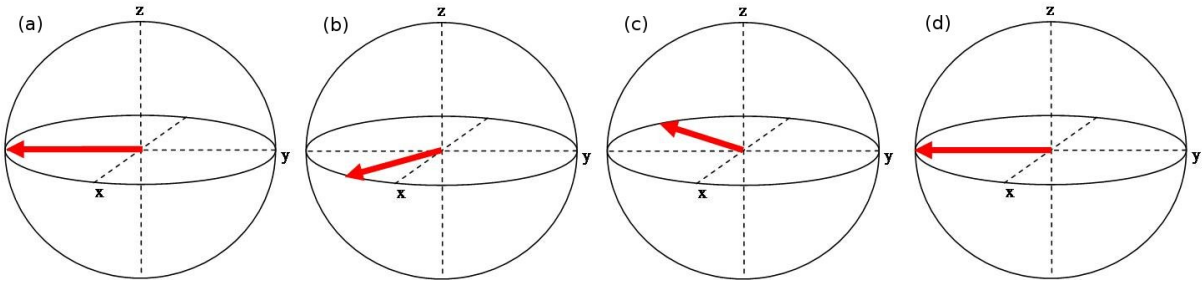


Figure 4.2: Due to J-coupling with another spin, the depicted spin will precess in the rotating frame. b) After a time $\frac{1}{2}\tau$ the spin has rotated through an angle $\theta$. c) The spin is then rotated by 180° around the y-axis and d) allowed to evolve for $\frac{1}{2}\tau$, during which it rotates through an angle $\theta$ back to it original position [15].

## 4.4 Gradients

On most modern spectrometers it is possible to apply an additional magnetic field in the z-direction that linearly depends on the z position. The Hamiltonian for a single spin in such a gradient in the spins individual rotating frame is

$$H_{grad} = -\frac{1}{2}\gamma B_1 zZ = \frac{1}{2}\omega_g zZ. \tag{4.6}$$

Consider that the spin is in the state $\rho = \alpha I + \beta Z + \gamma I^+ + \delta I^-$ where $I^+$ and $I^-$ are termed coherences and given by

$$I^+ = \begin{pmatrix} 0 & 1 \\ 0 & 0 \end{pmatrix} \quad I^- = \begin{pmatrix} 0 & 0 \\ 1 & 0 \end{pmatrix}. \tag{4.7}$$

Under the action of the gradient the different components of $\rho$ evolve as

$$e^{-i\omega_g zt\frac{Z}{2}}\alpha I e^{i\omega_g zt\frac{Z}{2}} = \alpha I \tag{4.8}$$

$$e^{-i\omega_g zt\frac{Z}{2}}\alpha Z e^{i\omega_g zt\frac{Z}{2}} = \beta Z \tag{4.9}$$

$$e^{-i\omega_g zt\frac{Z}{2}}\alpha I^{\pm} e^{i\omega_g zt\frac{Z}{2}} = e^{\mp 2i\omega_g zt} I^{\pm}. \tag{4.10}$$

Averaged over a sample of height $2l$, $\rho$ evolves as

$$\rho = \alpha I + \beta Z + \gamma I^+ + \delta I^- \quad \longrightarrow \quad \alpha I + \beta Z + \frac{1}{2l}\frac{\sin 2\omega_g lt}{2\omega_g lt}(\gamma I^+ + \delta I^-) \tag{4.11}$$

$$= \quad \alpha I + \beta Z \quad \text{for large } t. \tag{4.12}$$

Similarly, for two spins the $I$ and $Z$ terms are unaffected by the gradient while the $I^\pm$ terms evolve as

$$\begin{aligned} e^{-i\omega_g^1 tz(\frac{Z}{2}I)-i\omega_g^2 tz(I\frac{Z}{2})}(\alpha I^+ + \beta I^-) \otimes (\gamma I^+ + \delta I^-) e^{+i\omega_g^1 tz(\frac{Z}{2}I)+i\omega_g^2 tz(I\frac{Z}{2})} \\ = \alpha\gamma e^{-2itz(\omega_g^1+\omega_g^2)} I^+ I^+ \\ \alpha\delta e^{-2itz(\omega_g^1-\omega_g^2)} I^+ I^- \\ \beta\gamma e^{-2itz(-\omega_g^1+\omega_g^2)} I^- I^+ \\ \beta\delta e^{-2itz(-\omega_g^1-\omega_g^2)} I^- I^-. \end{aligned} \tag{4.13}$$

Note that if $\omega_g^1 \approx \omega_g^2$ (as is the case for homonuclear systems with typical gradient strengths) the zero coherences ($I^+I^-$ and $I^-I^+$) lose their z-dependent evolution and are not averaged away during a gradient. In general, only the coherences with equal number of same species spins in the $I^+$ and $I^-$ survive the gradient.

Note that evolution due to J-coupling is neglected during gradients because the $ZZ$ interaction does not change the coherence order. As most gradients are used to eliminate non-zero coherences, J-coupling does not affect the outcome. J-coupling can affect the desired evolution of the state for certain zero coherences, such as those contained in $IXX + IYY$, or when the gradient is used as a coherence filter. Therefore to minimize the J-coupling effect gradients are kept as short as possible.

This experiment uses gradients for two purposes. First, as crusher gradients to eliminate polarization in the xy-plane. Second, as a coherence filter in the pseudo-pure state preparation.

*Crusher Gradients*

As can be seen from equation 4.11, if $\omega_g t$ is large enough, non-zero coherences become wound in such a way as to average to zero, provided that they are not subsequently unwound by another gradient.

*Coherence Filter*

It is possible to unwind the effect of a gradient by using another gradient to cancel the z-dependent $Z$-rotation. Because of the spatial dependence of the winding, the second gradient must be applied before diffusion randomizes the locations of the molecules in the sample. This technique allows one to implement a spatial coherence filter as outlined below.

An n-coherence filter can be implemented with the following steps. Note that $\gamma_i$ is the gyromagnetic ratio of the $i^{th}$ spin and that factors of $\frac{1}{2}$ have been omitted for clarity.

1. Prepare an n-coherence (Ex. $I^+I^+I^+$).
2. Apply a gradient (Ex. $I^+I^+I^+ \longrightarrow e^{-i2ztB_1(\gamma_1+\gamma_2+\gamma_3)}I^+I^+I^+$).
3. Convert the n-coherence to a single coherence (Ex. $e^{-i2ztB_1(\gamma_1+\gamma_2+\gamma_3)}I^+I^+I^+ \longrightarrow e^{-i2ztB_1(\gamma_1+\gamma_2+\gamma_3)}(I+Z)(I+Z)I^+$).
4. Apply a second gradient to unwind the previously acquired phase (Ex. $e^{-i2ztB_1(\gamma_1+\gamma_2+\gamma_3)}(I+Z)(I+Z)I^+ \longrightarrow e^{-i2ztB_2(\gamma_3)}e^{-i2ztB_1(\gamma_1+\gamma_2+\gamma_3)}(I+Z)(I+Z)I^+$).

   In order for the acquired phases to cancel the condition

$$t_1B_1(\gamma_1+\gamma_2+\gamma_3)+t_2B_2\gamma_3=0 \tag{4.14}$$

   must be met. Typically $t_1=t_2$ such that

$$B_2=-B_1(\gamma_1+\gamma_2+\gamma_3)/\gamma_3. \tag{4.15}$$

As shown in the next section, the coherence filter can be used to create a labeled pseudo-pure state.

## 4.5 Initial State Preparation

In addition to a set of universal gates, QIP requires the ability to initialize a fiducial state. Typically in NMR a labeled pseudo-pure state is used as the fiducial state. The deviation

matrix of the thermal state can be transformed to a labeled pseudo-pure state of the form $X \bigotimes_i 0_i$ where $0 = \frac{1}{2}(I + Z)$ and $1 = \frac{1}{2}(I - Z)$ as outlined below [13].

1. Eliminate polarization on all but one spin (Ex $ZII$).
2. Apply a unitary to create a state that contains the highest order coherences (Ex. $YYX$).
3. Use a coherence filter to pass the highest coherences while eliminating all other coherences (Ex. $X00$).

# Chapter 5

# Control Techniques

## 5.1 Introduction

In quantum computing, logic gates are implemented as unitary operators acting on the qubits. In NMR implementations these unitary operators are realized by a sequence of radio-frequency pulses and the natural evolution of the spin system. In general, the pulse sequence that generates a desired unitary propagator is neither trivial nor unique. It is beneficial to find optimal sequences that minimize the negative effects of errors, relaxation, and decoherence.

For control purposes it is useful to divide the Hamiltonian into a component that describes the dynamics of the system, $H_s$, and a component that describes the control Hamiltonian, $H_c$. Furthermore, it is generally reasonable to assume that $H_c$ depends linearly on the control fields, $f_n(t)$. Therefore the Hamiltonian can be expressed as

$$H = H_s + H_c = H_s + \sum_{k=1}^{K} f_k(t) H_k. \tag{5.1}$$

The techniques for controlling nuclear magnetic resonance systems accurately and efficiently can be divided into two categories.

1. Determining the appropriate control fields to accurately implement a finite set of desired unitaries on low dimensional subsystems. Essentially this corresponds to

finding the correct radio-frequency control pulses.

2. Combining the individual pulses into a sequence that, when combined with the natural evolution of the system, efficiently implements a desired algorithm while minimizing the accumulation of error.

## 5.2 Pulses

The pulses used in this experiment can be categorized as follows. See Figures 5.1 for amplitude and phase diagrams for pulses from each category.

*Hard Pulses*

The simplest pulses used, they ideally consist of a constant amplitude and phase that are instantly turned on and off. These pulses are typically short with broad frequency response profiles.

*Composite Pulses*

By combining several hard pulses into a single composite pulse it is possible to construct an overall pulse with customized parameters. For example, it is possible to construct a composite 180° pulse from five 180° hard pulses that has a larger excitation profile than a single hard pulse. This idea can be extended to construct pulses that are divided into many time steps, each with a constant amplitude and phase [9]. Theoretically it is possible to implement arbitrary unitaries with such techniques, however the GRAPE algorithm (see below) generally gives better results.

*Soft Pulses*

Analytically derived soft (shaped) pulses with continually varying amplitudes and/or phases provide another useful pulse category. Typically, simple Gaussian pulse shapes are used with low power in order to optimize frequency selectivity. However, more complex shapes have been developed to address relevant issues such as universality, robustness to experimental imperfections, and required power [23, 10]. Due to the relative simplicity of the shape, a soft pulse drives the system through a simple trajectory, allowing the system's response to be easily determined. Consequently, it is easy to use these pulses in many

different situations by only varying the duration and frequency of the pulse to fit one's need.

*GRAPE*

By using numerical optimization techniques to search for the control fields, it is possible to extend the idea of composite pulses to include many time steps, dramatically increasing one's control over the system. As these techniques rely on simulating the full system dynamics for each time step, they can internally refocus off-resonant effects and unwanted J-couplings. However the search can be complex, growing linearly with the number of time steps and exponentially with the number of spins in the system. Gradient Ascent Pulse Engineering (GRAPE) is a fast way to search for such complex pulses [12]. The GRAPE method consists of discretizing the propagator $U$ into $N$ equal time steps of length $\Delta t$ during which the control Hamiltonian is constant. Therefore, the system evolution during time step $j$ is given by

$$U_j = e^{-i\Delta t\left(H_s+\sum_{k=1}^{K} f_k(j)H_k\right)}. \tag{5.2}$$

The density operator at time $T = N\Delta t$ is given by

$$\rho(T) = U_N ... U_1 \rho_0 U_1^\dagger .... U_N^\dagger. \tag{5.3}$$

The goal of the GRAPE algorithm is to find the optimal RF control fields that take an initial state, $\rho_0$, to a final state, $\rho(T)$, in a time $T$ that maximizes the overlap of $\rho(T)$ with $\rho_{goal}$ defined by the fitness function [12]

$$\Phi = tr(\rho_{goal}^\dagger \rho(T)). \tag{5.4}$$

$\Phi$ can be expressed using a backward propagated $\rho_{goal}$ and $\rho_j$, the state at time step $j$

$$\Phi = tr(\underbrace{U_{j+1}^\dagger \dots U_N^\dagger \rho(T) U_N \dots U_{j+1}}_{A_j} \underbrace{U_j \dots U_1 \rho_0 U_1^\dagger \dots U_j^\dagger}_{\rho_j}). \tag{5.5}$$

The GRAPE algorithm consists of the following:

1. Guess the initial control fields $f_k$.

2. Calculate $\rho_j$ and $A_j$ for all $j \leq N$.

3. Evaluate $\frac{\delta\Phi}{\delta f_k(j)}$ and update the control parameters $f_k(j)$ according to $f_k(j) \rightarrow f_k(j) + \epsilon\frac{\delta\Phi}{\delta f_k(j)}$ where $\epsilon$ is a predetermined small step. With the new control parameters go to step 2.

The search is completed when the change in $\Phi$ is below a chosen threshold.

Through clever calculation of $\frac{\delta\Phi}{\delta f_k(j)}$, the GRAPE algorithm significantly reduces the number of propagator time evolutions that need to be calculated [12], compared to previous methods. This enables numerical optimizations over larger parameters spaces, such as more time steps or spins. It is possible to adjust the fitness function and search algorithm such that the optimized pulses are robust to small RF power inhomogeneities and/or chemical shift variances, with only a linear cost in search time. See Figure 5.2 for sample robustness curves. Furthermore, it is possible to adjust the algorithm such that unitary propagators are found that work correctly on all input states.

## 5.3 Sequence Compilation

Although it is theoretically possible to use numerical optimization techniques, such as GRAPE, to implement an arbitrary unitary, the exponential increase in computational search time with system size limits their use to small systems. Furthermore, computational constraints often limit the GRAPE algorithm to simple unitaries where a reasonable number of time steps can be used (ex. a 90° rotation versus an entire quantum circuit). One method to address this is to use numerically optimized pulses on subsets of the system. These pulses are then combined to implement the desired total unitary, in a way that minimizes the accumulation of errors. Such errors include coupling during and between pulses and phase shifts on off-resonant spins due to the Block-Siegert effect [23]. Note that even numerically optimized pulses may not completely refocus undesired evolutions. Also, if GRAPE is implemented on a subsystem it will not correct the undesired evolution of the other subsystems.

One approach to handle these errors is to decompose a pulse into an ideal pulse preceded

and followed by phase and coupling errors to account for the Bloch-Siegert effect, chemical shift evolution, and ZZ-couplings during the pulse [1]. Explicitly, the unitary evolution of the pulse can be decomposed as

$$\begin{aligned} U_{pulse} &= e^{-i(H_{rf}+\sum_i(\omega_i Z_i)+\sum_{i<j}(\frac{\pi}{2}J_{ij}Z_iZ_j))\Delta t} && (5.6)\\ &\approx U^{post}_{Zerror}U^{post}_{ZZerror}U_{ideal}U^{pre}_{ZZerror}U^{pre}_{Zerror} && (5.7)\\ &= \prod_i e^{-i\alpha_i Z_i}\prod_{i<j}e^{-i\beta_{ij}Z_iZ_j}e^{-iH_{rf}\Delta t}\prod_{i<j}e^{-i\gamma_{ij}Z_iZ_j}\prod_i e^{-i\delta_i Z_i}. && (5.8)\end{aligned}$$

By using single spin and pairwise simulations, the pulse decomposition can be accomplished efficiently. Once the pre and post errors are known, it is possible to design a pulse sequence that minimizes the total error. Individual rotating frames are used for each spin, meaning that $Z$-rotation errors can be absorbed by a reference frame change. The ZZ-coupling is tracked so that it is possible to insert refocusing pulses when needed. Pulse sequence compilation is achieved using software that takes as input the system Hamiltonian, the effective pulse decompositions, a refocusing scheme, and the desired pulse sequence. It then numerically optimizes the timing and phases of the pulses to most accurately implement the desired pulse sequence.

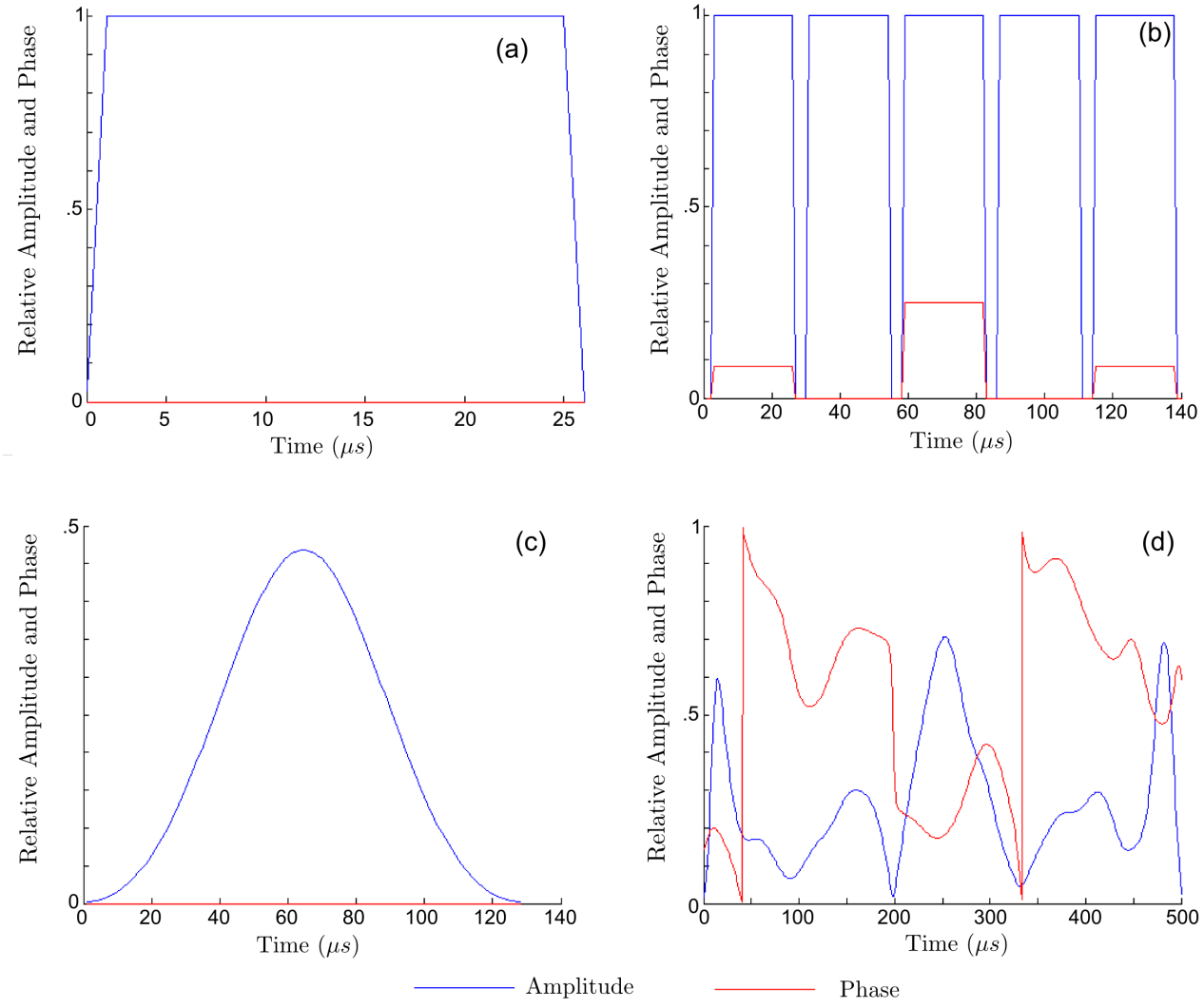


Figure 5.1: Examples of amplitude and phase plots for various pulse types. The amplitude is relative to the maximum experimentally calibrated power and the phase is a fraction of 360°. (a)A hard 180° pulse. (b) A 180° composite pulse with a broader uniform frequency response. (c) A soft frequency selective pulse derived from the inverse hyperbolic secant. (d) A GRAPE pulse that implements a 180° pulse on the Methyl group of trans-crotonic acid - See Section 6.2

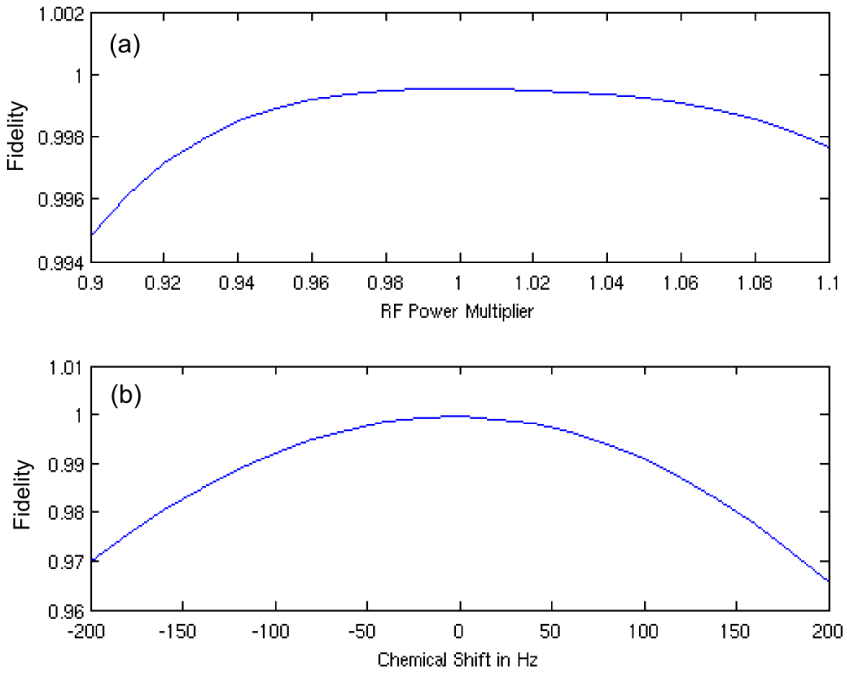


Figure 5.2: Trace fidelities for the Methyl 180° GRAPE pulse depicted in Figure 5.1 for variations in (a) RF power and (b) chemical shift. The flat profiles for small variations indicate that the pulse is robust to small changes in the system Hamiltonian, RF field inhomogeneities, and miscalibration.

# Chapter 6

# NMR Implementation and Simulations

## 6.1 Introduction

The following section outlines an NMR implementation of the magic state distillation and the relevant simulations that were conducted to test its experimental feasibility.

## 6.2 System

As the distillation requires 5 qubits, a suitable NMR system consists of 6 spins, 5 for the distillation algorithm and an additional spin to enable the initial state preparation. The six spins must have sufficiently different resonant frequencies to be individually addressable, yet adequately coupled to their neighboring spins to allow the necessary 2-qubit gates. Furthermore, the peaks of the observation spins must be sufficiently separated to enable the successful extraction of observable terms. A system that meets all of these requirements is carbon-13 labeled trans-crotonic acid in the liquid state (See Figure 6.1 and 6.2). Although trans-crotonic acid contains 7 spins (the methyl group is treated as a single spin) the additional challenges due to the extra spin are outweighed by the positive characteristics of the molecule.

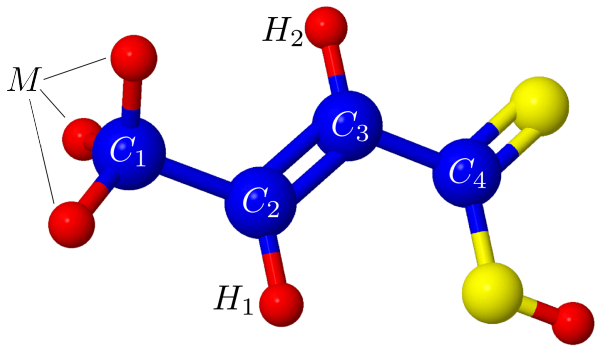


Figure 6.1: Molecular structure of trans-crotonic acid. The labeled spins correspond to the qubits used in the magic state distillation.

## 6.3 Pulses

The system is controlled using the pulses listed in Table 6.1. Certain pulses, such as M90 and C490, are also used in parallel. The GRAPE pulses are optimized to be robust to typical RF amplitude fluctuations and chemical shift variations.

## 6.4 Experiment Overview

The NMR implementation of the magic state experiment can be divided into three main stages as depicted in Figure 6.3. Note that spin states are given in density operator form with the spins ordered as $H_1H_2C_1C_2C_3C_4M$.

1. State Preparation - Preparation of $|T^{enc}\rangle\langle T^{enc}|$ from the thermal state.

2. Distillation - Transformation of the faulty input state to a state that includes one distilled magic state.

3. Measurement - Unitary transformation of the distilled magic state to observable terms and the extraction of the final purity and success probability.

Table 6.1: Pulses used in the magic state distillation.

| **Pulse Name** | **Type** | **Duration ($\mu s$)** | **Target Spin** | **Rotation Angle** | **Fidelity**[1] |
|---|---|---|---|---|---|
| *Proton* | | | | | |
| Hh90 | Hard | 12 | M, $H_1$, $H_2$ | 90 | 1.0000 |
| Hhc180 | Composite | 140 | M, $H_1$, $H_2$ | 180 | 0.9998 |
| M90 | GRAPE[2] | 400 | M | 90 | 0.9988 |
| M180 | GRAPE[2] | 500 | M | 180 | 0.9966 |
| H190 | GRAPE | 600 | $H_1$ | 90 | 0.9970 |
| H1180 | GRAPE | 1000 | $H_1$ | 180 | 0.9979 |
| H290 | GRAPE | 600 | $H_2$ | 90 | 0.9981 |
| H2180 | GRAPE | 1000 | $H_2$ | 180 | 0.9967 |
| *Carbon* | | | | | |
| C190 | soft | 128 | $C_1$ | 90 | 0.9998 |
| C1180 | soft | 128 | $C_1$ | 180 | 0.9991 |
| C290 | soft | 700 | $C_2$ | 90 | 0.9996 |
| C2180 | soft | 700 | $C_2$ | 180 | 0.9944 |
| C390 | soft | 700 | $C_3$ | 90 | 0.9996 |
| C3180 | soft | 700 | $C_3$ | 180 | 0.9939 |
| C490 | soft | 700 | $C_4$ | 90 | 0.9996 |
| C4180 | soft | 700 | $C_4$ | 180 | 0.9986 |
| *Specialty* | | | | | |
| MCall2 | GRAPE | 100 | M,$C_1$,$C_2$,$C_3$,$C_4$ | 30.67 | 0.9985 |
| MCall3 | GRAPE | 150 | M,$C_1$,$C_2$,$C_3$,$C_4$ | 40.72 | 0.9995 |
| MCall4 | GRAPE | 250 | M,$C_1$,$C_2$,$C_3$,$C_4$ | 51.66 | 0.9985 |
| MCall5 | GRAPE | 250 | M,$C_1$,$C_2$,$C_3$,$C_4$ | 64.30 | 0.9983 |
| Trot | GRAPE | 250 | M,$C_1$,$C_2$,$C_3$,$C_4$ | 54.72 | 0.9980 |
| rfsel64H | Composite | 11592 | M | 0,180[3] | -[4] |

[1] Fidelity is the simulated fidelity of the pulse given perfect correction of the error terms of the pulse decomposition. See section 5.3

[2] The methyl GRAPE pulses are subsystem pulses applied only to the protons, while all other GRAPE pulses are parallel pulses composed of a proton and carbon component.

[3] The angle of rotation is dependent on phase cycling.

[4] The fidelity of the rfsel64H pulse could not be calculated due to limitations in the simulation software.

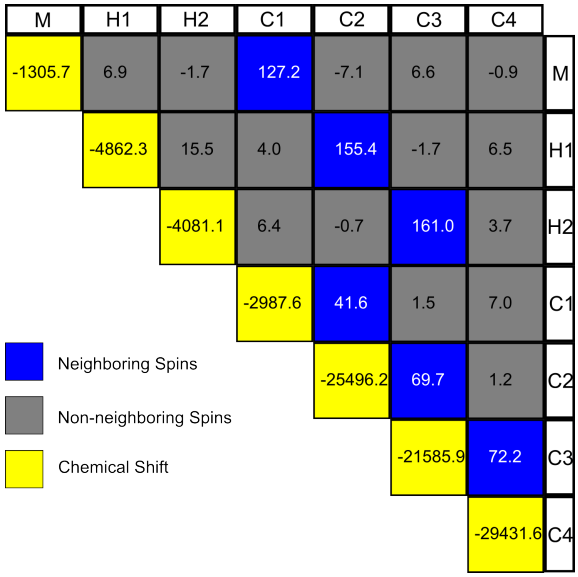


Figure 6.2: Properties of trans-crotonic acid. Chemical shift values (Hz) are on the diagonal with respect to reference frequencies of 700.13 MHz for protons and 176.05 MHz for carbons. J-coupling values (Hz) are off-diagonal.

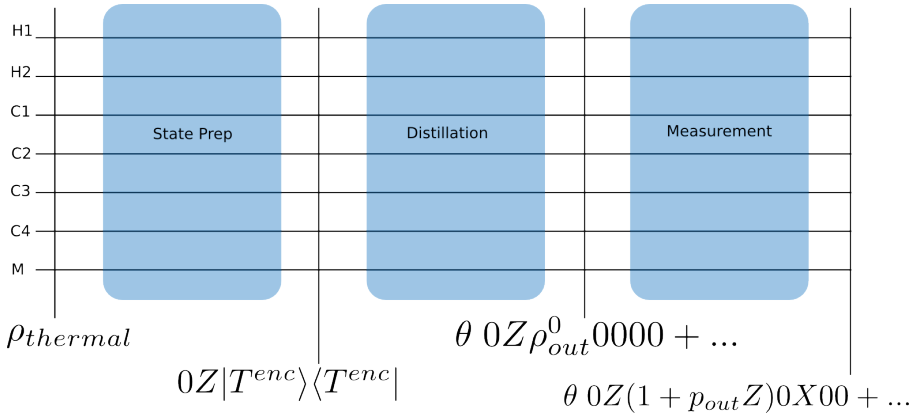


Figure 6.3: Circuit diagram overview of the experiment with the ideal spin states listed for the various stages.

## 6.5 State Preparation

The state preparation stage can be further divided into six steps as shown in Figure 6.4.

a. RF selection - Selection of a physical subset of spins that responds uniformly to the applied control fields.

b. Crushing - Elimination of all but the methyl polarization.

c. Methyl spin-$\frac{1}{2}$ selection - Selection of the spin-$\frac{1}{2}$ subspace of the methyl group.

d. Pseudo-pure state preparation - Creation of a labeled pseudo-pure state using spatial averaging.

e. Depolarization - Mixing of the pseudo-pure state to create 'faulty' states.

f. T-rotation - Rotation of M, $C_1$, $C_2$, $C_3$, and $C_4$ into the state $|T^{enc}\rangle\langle T^{enc}|$.

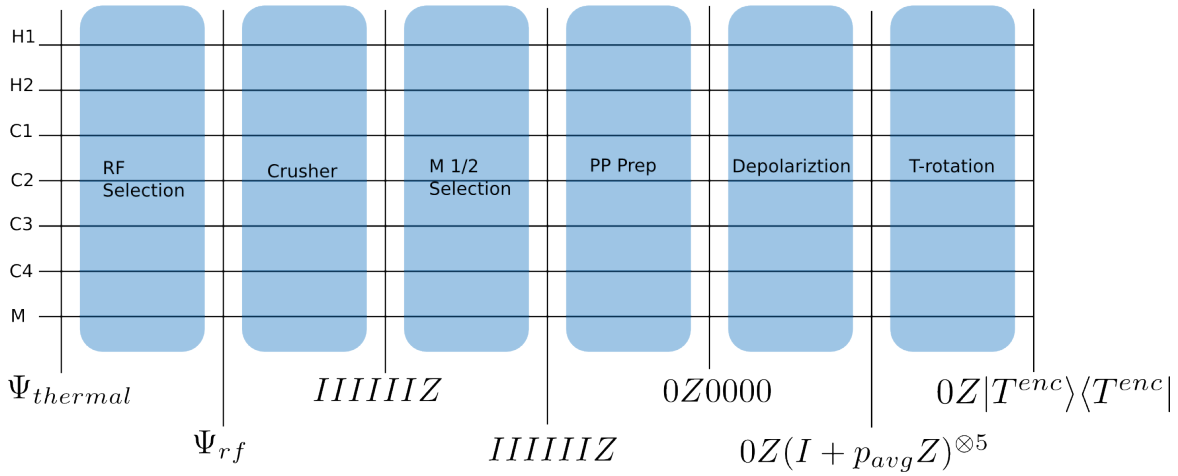


Figure 6.4: State preparation overview with the ideal spin states listed for the different stages.

### 6.5.1 RF Selection

Although modern spectrometers are highly precise instruments, small variations in the RF magnetic field can occur over the space of the sample. These variations can arise from coil geometries, sample imperfections, etc. The result is that spins in different physical locations experience varying fractions of the total RF power, and consequently nutate at varying rates. These RF inhomogeneities can give rise to pulse imperfections.

The dependency of the nutation rate on RF power means that it is possible to use a pulse sequence to select a physical subset of spins that experience similar RF power. To implement RF selection a composite pulse is used consisting of the sequence $90^\circ_x - (180^\circ_{-x})^{64} - (180^\circ_{\theta_i} - 180^\circ_{-\theta_i})^{64} - 90^\circ_y$ where the phases $\theta_i$ are chosen from a 64 point Gaussian where $\sum_{i=1}^{64} \theta_i = 22.5^\circ$ [13]. Each experiment is repeated with a second sequence that effectively replaces $\theta_i$ with $-\theta_i$. The two experiments are added to eliminate the unwanted signal due to the 'shoulder' terms of the signal response. See Figure 6.5 for a plot of the signal response after using RF selection. Note that because only a subset of spins is selected, the total amount of signal decreases when using RF selection.

### 6.5.2 Polarization Crushing

The goal of the crusher sequence is to take the thermal deviation matrix (after RF selection) to the state $IIIIIIZ$. This is accomplished by rotating all the spins except the methyl group into the plane, followed by a crushing gradient. See Figure 6.6 for the pulse sequence.

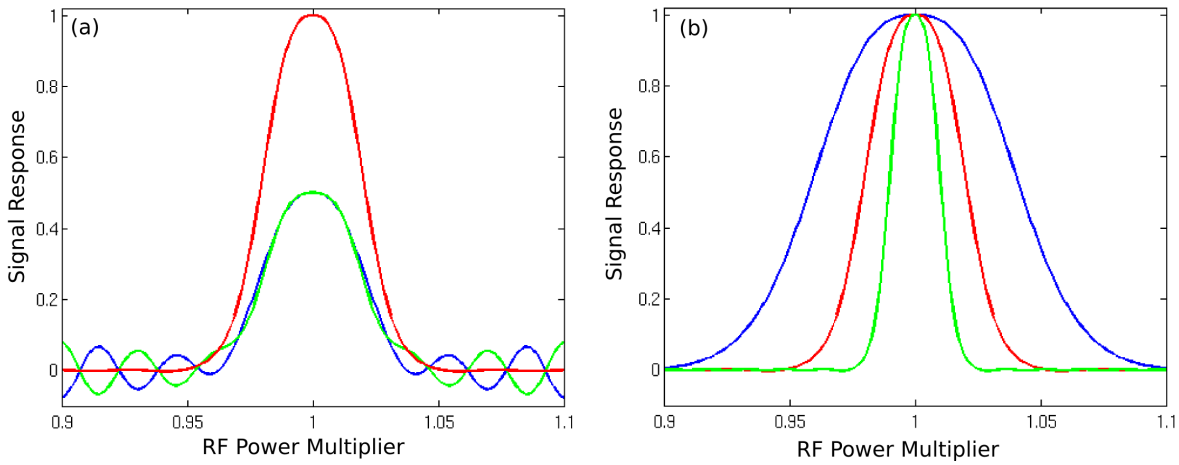


Figure 6.5: (a) Signal response for the two RF selection pulses and the sum of the signal response. (b) Comparison of signal response to RF selection for composite pulses using 32 (blue), 64 (red), and 128 (green) point Gaussians for the rotation angles. The 64 point distribution was chosen as a balance of RF selectivity and pulse duration. See Section 6.5.1
.

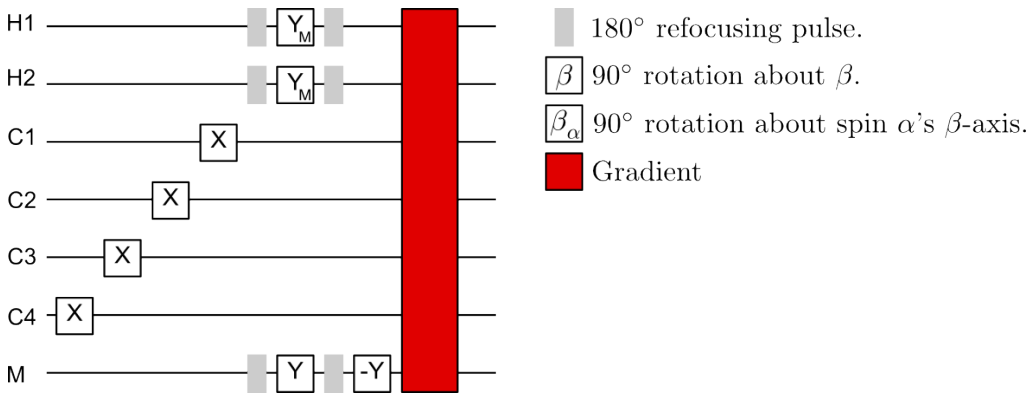


Figure 6.6: Polarization crushing pulse sequence.

### 6.5.3 Methyl Spin-$\frac{1}{2}$ Selection

Although not equivalent to a single spin-$\frac{1}{2}$ particle the methyl group of trans-crotonic acid can be used for QIP by using a pulse sequence to isolate the spin-$\frac{1}{2}$ subspace. Adding the methyl's three equivalent protons results in a spin system with a spin-$\frac{3}{2}$ and spin-$\frac{1}{2}$ components. The pulse sequence that selects the spin-$\frac{1}{2}$ subspace is shown in Figure 6.7. This sequence transforms the spin-$\frac{3}{2}$ subspace to a state that is crushed by the gradient while passing the transformed spin-$\frac{1}{2}$ subspace. For simplicity the pulse sequence is simulated on a test system composed of a methyl group and a single carbon. Prior to the spin-$\frac{1}{2}$ selection sequence the carbon spectrum corresponds to equivalent coupling to three spin-$\frac{1}{2}$ particles. After the pulse sequence the spectrum is equivalent to a single coupling and corresponds to selecting the spin-$\frac{1}{2}$ subspace of the methyl group. See Figure 6.8. If implemented ideally the sequence retains 99.7% of the spin-$\frac{1}{2}$ signal while effectively eliminating the spin-$\frac{3}{2}$ signal.

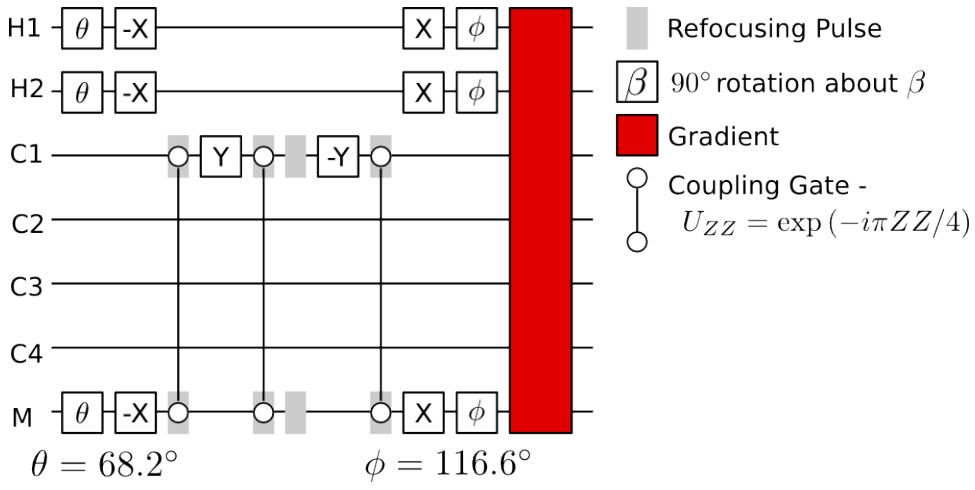


Figure 6.7: Methyl spin-$\frac{1}{2}$ selection pulse sequence.

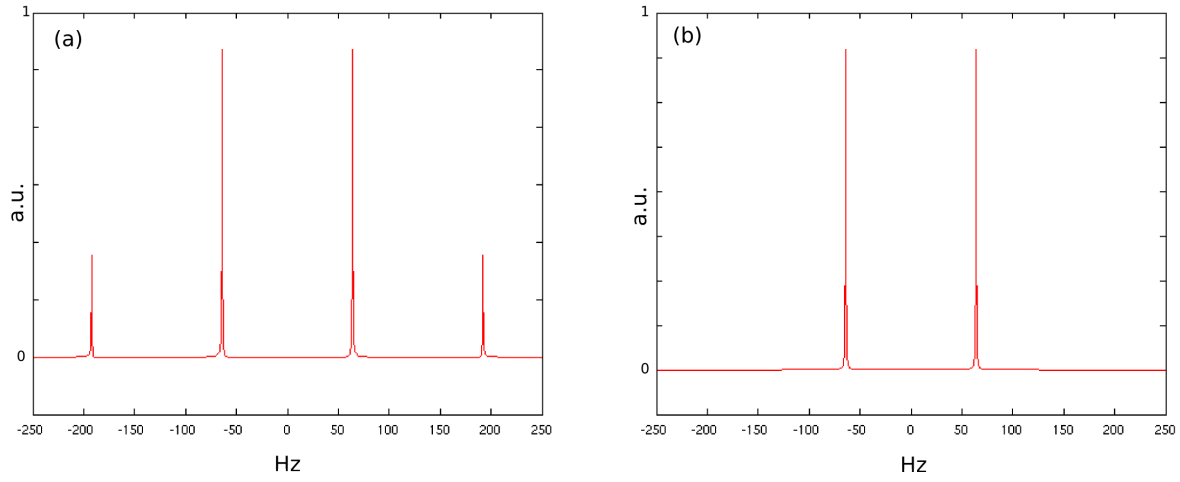


Figure 6.8: (a) Carbon spectrum prior to methyl spin-$\frac{1}{2}$ selection. Notice the 1-3-3-1 ratio of the peaks corresponding to the three equivalent protons. (b) Carbon spectrum after methyl spin-$\frac{1}{2}$ selection. The spectrum is now equivalent to the spectrum of carbon coupled to a single spin-$\frac{1}{2}$ particle.

### 6.5.4 Labeled Pseudo-Pure State Preparation

The labeled pseudo-pure state preparation stage takes the state $IIIIIIZ$ to $0Z00000$ through the use of the spatial coherence filter method described in section 4.5. The encoding sequence creates the state $XXXXXXX$, which contains 7-coherence terms, and applies a spatially dependent Z-rotation with the gradient. The decoding sequence transforms the wound 7-coherence terms to the single coherence terms contained in $0X00000$. A gradient is then applied that unwinds the desired terms while averaging away the others. The ratio of decoding to encoding gradients is given by

$$\frac{-\left(\gamma_{H1}+\gamma_{H2}+\gamma_{C1}+\gamma_{C2}+\gamma_{C3}+\gamma_{C4}+\gamma_{M}\right)}{\gamma_{H2}} \approx -4.0058 \tag{6.1}$$

where $\gamma_i$ is the gyromagnetic ratio of the $i^{th}$ spin. The decoding gradient is followed by an H290 pulse, which takes the state to $0Z00000$, and a clean up gradient that crushes any non-zero coherence error terms. See Figure 6.9. The fidelity of the simulated pseudo-

pure state, as defined in Section 6.9, is approximately 98%. The spectra of the simulated state, after a readout pulse, is given in Figure 6.10. Note that the selected peak is not the rightmost peak due to the negative coupling of $H_2$ to $M$ and $C_2$.

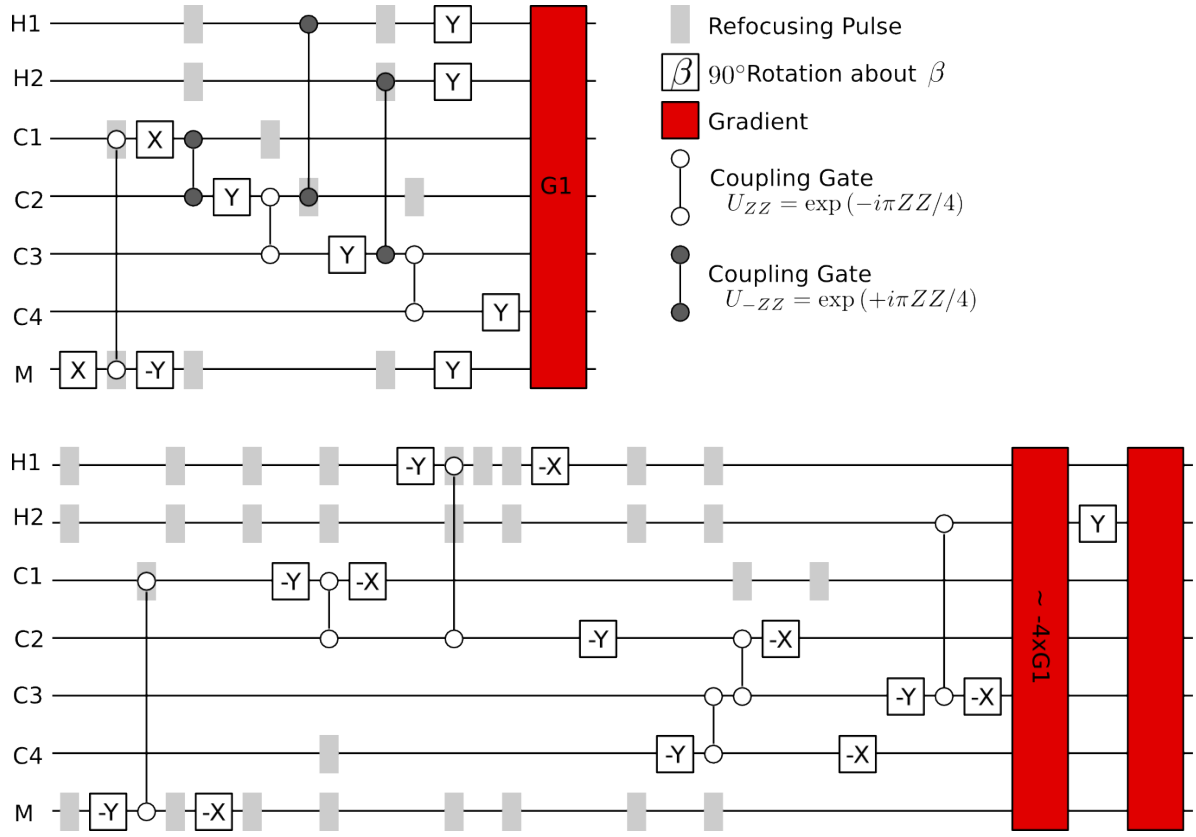


Figure 6.9: Pseudo-pure encoding (top) and decoding (bottom) pulse sequences.

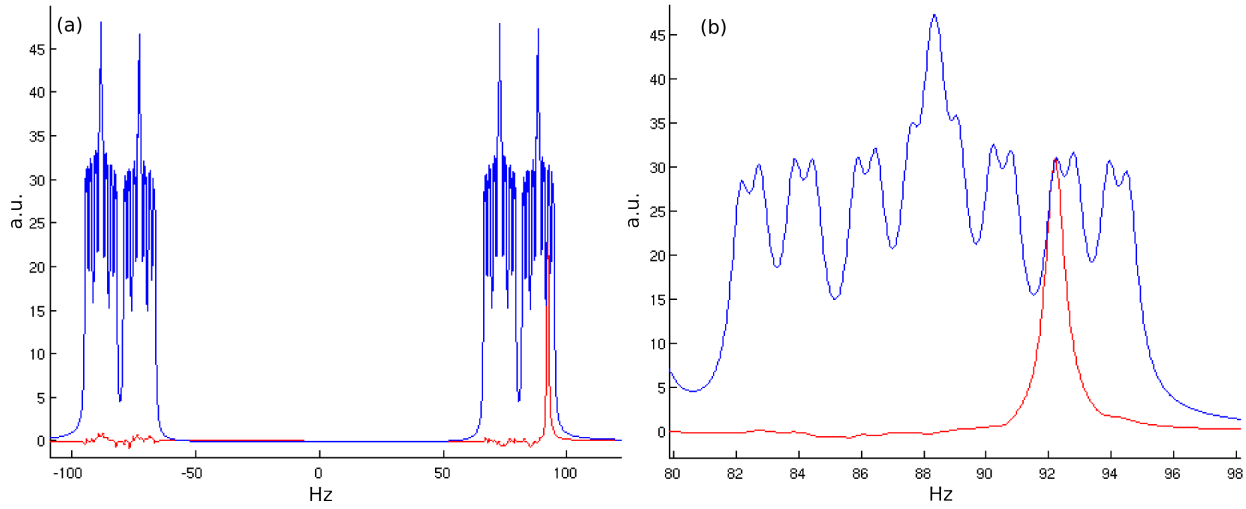


Figure 6.10: Simulated $H_2$ pseudo-pure and thermal reference spectra. (a) Full spectra and (b) zoomed spectra.

### 6.5.5 Depolarization

As discussed, the distillation algorithm requires as input five states of the form

$$\rho_{in} = \frac{1}{2}\left[I + \frac{p_{avg}}{\sqrt{3}}(X + Y + Z)\right]. \tag{6.2}$$

Henceforth, $p_{avg}$ will be written as $p^i$ to indicate which spin is involved. The preparation of these faulty states is accomplished by depolarizing the pseudo-pure state and then rotating the faulty state to lie along the x+y+z direction. Depolarization is achieved by using a GRAPE pulse that collectively rotates $M$, $C_1$, $C_2$, $C_3$, and $C_4$ about the y-axis by an angle $\theta$. Therefore the state evolves from $0Z00000$ to $0Z(1+\cos(\theta)Z+\sin(\theta)X)^{\otimes 5}$ and the planar component is crushed with a gradient, leaving the state

$$0Z(I + \cos(\theta)Z)^{\otimes 5} + \rho_{zero}. \tag{6.3}$$

$\rho_{zero}$ is the sum of all zero coherence terms of the form $0ZA_1A_2A_3A_4B$ where $A_i$ is chosen from $I, Z, I^+, I^-$ and $B$ chosen from $I, Z$ with the condition that the number of $I^+$ is

equal to the number of $I^-$. Zero coherences which include the methyl are crushed by the gradient due to the large Larmor frequency difference between protons and carbons. As demonstrated in Section 6.7 the zero coherence terms have negligible affect on the distillation. The sequence is conducted for $\theta \approx 0,\ 30.7,\ 40.7,\ 51.7$ and 64.3.

The amount of depolarization achieved can be measured by rotating $C_1$ into the plane and observing the spectrum. See Figure 6.12 for the relevant spectra. After fitting the spectrum the $p^i$ values are determined by searching the parameter space for the values that minimize an appropriate distance function. See Table 6.2 for the complete list of observables and scaling factors. The extracted depolarization values are plotted in Figure 6.14.

Although feasible for simulations, the above approach is experimentally difficult due to the small size of the peaks relative to error terms. This is best illustrated if one considers the relative amount of signal for each peak. Note that the terms in equation 6.3 of the form $(I+\cos(\theta)Z)^{\otimes 5}$ can be written as $((1+p^i)0+(1-p^i)1)^{\otimes 5}$. Therefore the depolarized scaling factor of each peak is given by

$$p^{C_1}(1 \pm p^{C_2})(1 \pm p^{C_3})(1 \pm p^{C_4})(1 \pm p^{M}) \tag{6.4}$$

where $p^i$ is either added or subtracted based on whether that spin is in the state 0 or 1 for that peak. To demonstrate the challenge presented by error terms it is sufficient to consider the ideal situation where all $p^i$'s are equal. Therefore the scaling factor can be calculated as

$$p^i(1+p^i)^{\gamma}(1-p^i)^{\delta} \tag{6.5}$$

where $\gamma$ is the number of spins $C_2$, $C_3$, $C_4$, and $M$ in the 0 state and $\delta$ is the number in the 1 state. As can be seen from Figure 6.13 error terms can significantly affect the intensity of all the peaks with one or more spins in the 1 state. This reduces the accuracy and reliability of this method for extracting the initial depolarization.

At best the distillation can increase the $p^i$ values by about 9%, meaning that there is not much tolerance for error in the initial $p^i$ values. Furthermore, as the extracted $p^i$ values are very sensitive to the presence of error terms, it is very difficult to evaluate how well the depolarization pulses are working.

An alternate approach to determine if the depolarization pulses are working correctly is to apply the pulses on the thermal state and individually observe the different spins, checking if the amount of signal loss corresponds to the correct rotation. As the pulses are unitary, if they work correctly on the thermal state they should work correctly for all input states, including the pseudo-pure state.

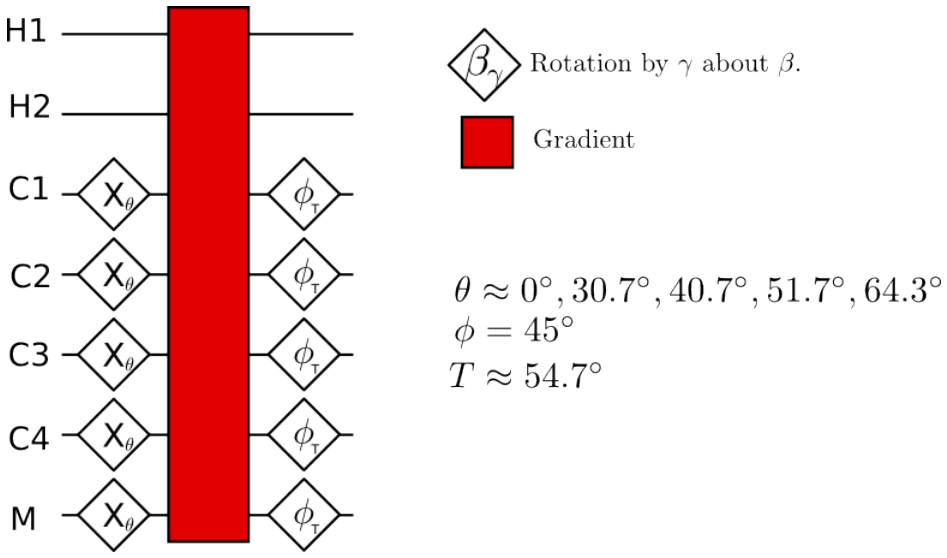


Figure 6.11: Depolarization and T-rotation pulse sequence

Table 6.2: Depolarization observables. The observables are determined by either fitting the simulated spectrum or analyzing the simulated density matrix. This is an over-specified system of equations so the $p^i$ values are determined by minimizing the distance of a fitness function to the measured observables.

| **Observable** | **Scaling Factor** |
|---|---|
| 0ZXIIII | $p^{C_1}$ |
| 0ZXZIII | $p^{C_1}p^{C_2}$ |
| 0ZXIZII | $p^{C_1}p^{C_3}$ |
| 0ZXZZII | $p^{C_1}p^{C_2}p^{C_3}$ |
| 0ZXIIZI | $p^{C_1}p^{C_4}$ |
| 0ZXZIZI | $p^{C_1}p^{C_2}p^{C_4}$ |
| 0ZXIZZI | $p^{C_1}p^{C_3}p^{C_4}$ |
| 0ZXZZZI | $p^{C_1}p^{C_2}p^{C_3}p^{C_4}$ |
| 0ZXIIIZ | $p^{C_1}p^{M}$ |
| 0ZXZIIZ | $p^{C_1}p^{C_2}p^{M}$ |
| 0ZXIZIZ | $p^{C_1}p^{C_3}p^{M}$ |
| 0ZXZZIZ | $p^{C_1}p^{C_2}p^{C_3}p^{M}$ |
| 0ZXIIZZ | $p^{C_1}p^{C_4}p^{M}$ |
| 0ZXZIZZ | $p^{C_1}p^{C_2}p^{C_4}p^{M}$ |
| 0ZXIZZZ | $p^{C_1}p^{C_3}p^{C_4}p^{M}$ |
| 0ZXZZZZ | $p^{C_1}p^{C_2}p^{C_3}p^{C_4}p^{M}$ |

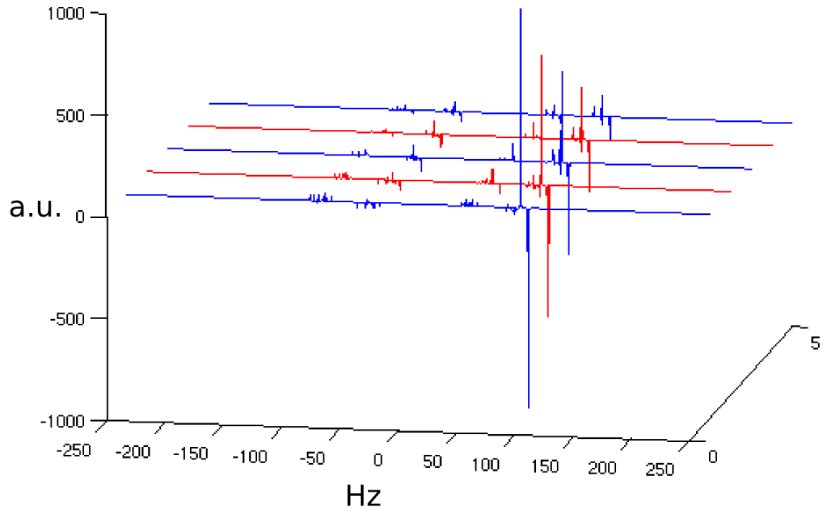


Figure 6.12: $C_1$ spectra after depolarization. Spectra 1 through 5 are for depolarization amounts $\theta \approx 0,\ 30.7,\ 40.7,\ 51.7$ and 64.3. Except for the two large peaks in each spectrum (corresponding to spins $C_2$, $C_3$, $C_4$, and $M$ being in the 0 state) all other peaks have a very small intensity (on the order of the error terms present in spectrum 1). Note that the coloring is for readability only.

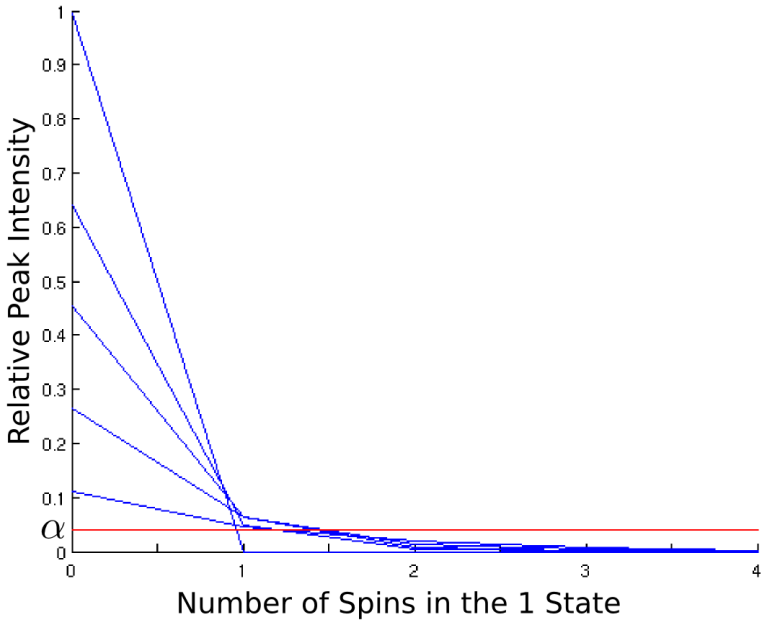


Figure 6.13: Relative ideal intensity of peaks in Figure 6.12 with 0 to 4 spins (chosen from $C_2$, $C_3$, $C_4$, and $M$) in the 1 state. The five blue curves correspond to the five different depolarization amounts. $\alpha$ is the approximate intensity of error term peaks as determined from the spectrum of the first depolarization experiment (ie $p^i = 1$). This figure demonstrates that each peak with at least one depolarized spin in the 1 state is significantly affected by error terms.

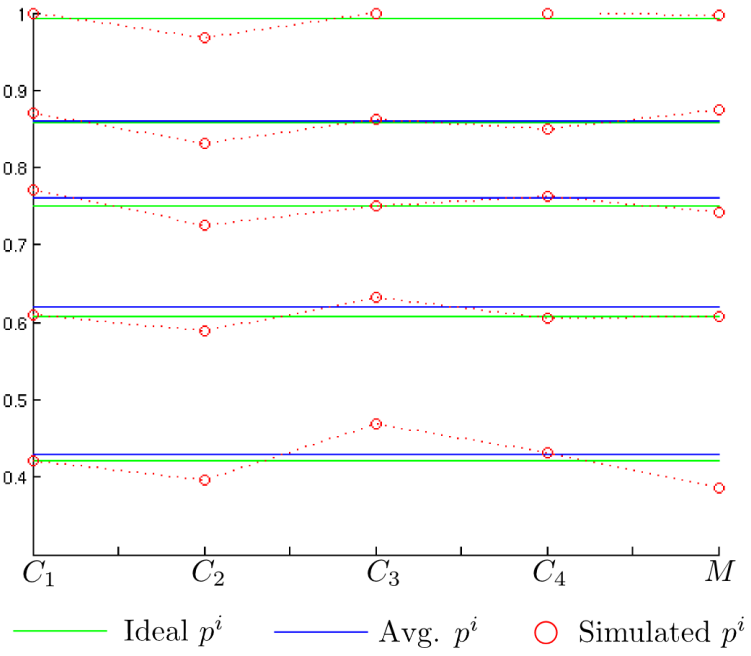


Figure 6.14: Simulated $p^i$ values as outlined in Section 6.5.5. Note that there is slight variation in the depolarization amounts between spins.

### 6.5.6 T-Rotation

The T-rotation step takes depolarized states of the form

$$\frac{1}{2^5}0Z(I+p^iZ)^{\otimes 5}+\rho_{zero} \tag{6.6}$$

to faulty magic states given by

$$\frac{1}{2^5}0Z\left[I+\frac{p^i}{\sqrt{3}}(X+Y+Z)\right]^{\otimes 5}+U_T\rho_{zero}U_T^\dagger \tag{6.7}$$

where $U_T$ is the collective rotation of $C_1C_2C_3C_4M$ by an angle of $\arccos\frac{1}{\sqrt{3}}\approx 54.7°$ about the x+y axis. See Figure 6.11 for the circuit. Like the depolarization pulses the T-rotation pulse is tested on the thermal state and assumed to work in the same manner on any input state.

## 6.6 Distillation

The distillation stage applies a unitary transformation that takes the five faulty magic states and probabilistically returns the states listed in the left of Table 6.3. The unitary transformation is very similar to the decoding sequence of the 5-qubit code. Due to the nature of the algorithm, $C_1$ contains the distilled magic state only when $C_2C_3C_4M$ are in the 0000 state. However, because NMR uses an ensemble system the final state is a mixture of all possible outcomes scaled by a factor, $\theta_i$, corresponding to the probability of that outcome. Therefore, rotating $C_1$ by 90° around $x+y$ followed by a $Z$-rotation of $-9.7356°$ produces the observable $\theta p_{out}\ 0ZX000$. The analytical expression for $\theta_0$ is given in equation 2.36. Both $\theta_0$ and $p_{out}$ depend on the fidelity of the experiment, meaning that a poor implementation could cause errors in $\theta_0$ and $p_0$ that offset each other preventing the reliable extraction of $p_{out}$.

## 6.7 Distillation Measurement

A solution to the distillation measurement problem is to transform the state to include two observables; one that is scaled by $\theta_0 p_{out}$ and the other by $\theta_0$. The ratio of these two

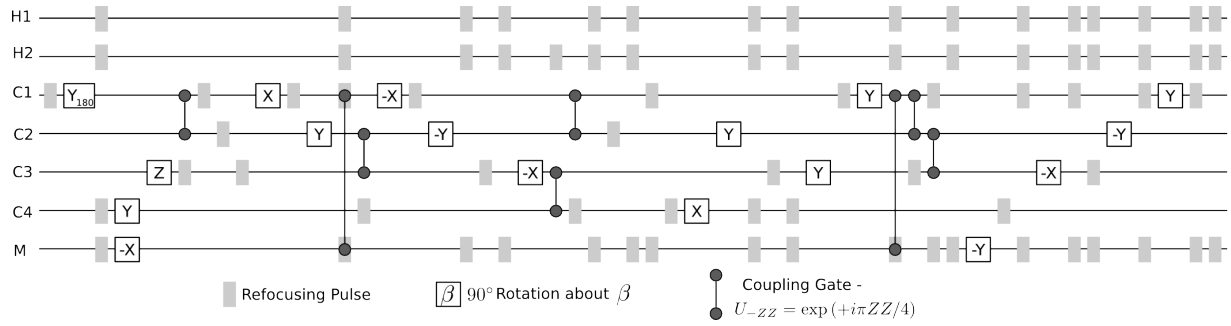


Figure 6.15: Distillation pulse sequence

observables yields $p_{out}$. One method that accomplishes this involves rotating $C_1$ to the state $(I + p_{out}Z)$, performing a conditional 90° rotation on $H_2$ when $C_3$ is in the state 1, and then rotating $C_3$ into the plane and observing $C_3$. This sequence transforms the terms in the left hand column of Table 6.3 to the terms in the right hand column. The transformed state includes the observables $0ZI0X00$ and $0ZZ0X00$ which are scaled by $\theta_0$ and $\theta_0 p_{out}$ respectively. Note that for technical reasons, such as virtual 180° pulses used in the sequence compiler, the desired observables are actually mapped to $\theta_0$ $0ZI0X11$ and $-\theta_0 p_{out}$ $0ZZ0X11$. The relevant peaks are separated by approximately 1.5Hz, which means that they are sufficiently resolved for $C_3$'s $T_2^*$ values as determined in Section 7.1.2. A thermal spectrum of $C_3$ is typically not well resolved as the couplings to $C_1$ and $H_1$ are approximately the same strength. However, in our situation $H_1$ is in the 0 state resulting in a resolved state with half as many peaks.

The distillation values are extracted by either fitting the simulated spectrum or analyzing the simulated density matrix. To determine the source of errors the distillation procedure is simulated from the various starting points and the extracted distillation values are plotted in Figure 6.17.

As the distillation is successful when starting from an ideal $|T^{enc}\rangle\langle T^{enc}|$ state, it indicates that the distillation and measurement pulse sequences work. Furthermore, because the distillation is successful when starting after the depolarization pulses, it indicates that the T-rotation pulse is working correctly and that the effect of zero coherences is negligible.

Table 6.3: Distillation output states before and after the measurement transformation.

| **Before Transformation** | **After Transformation** |
|---|---|
| $\theta_0\ 0Z\rho^0_{out}0000$ | $\theta_0\ 0Z(I+p_{out}Z)0(1+X)00$ |
| $\theta_1\ 0Z\rho^1_{out}0001$ | $\theta_1\ 0Z(I+p^1_{out}Z)0(1+X)01$ |
| $\theta_2\ 0Z\rho^2_{out}0010$ | $\theta_2\ 0Z(I+p^2_{out}Z)0(1+X)10$ |
| $\theta_3\ 0Z\rho^3_{out}0011$ | $\theta_3\ 0Z(I+p^3_{out}Z)0(1+X)11$ |
| $\theta_4\ 0Z\rho^4_{out}0100$ | $\theta_4\ 0X(I+p^4_{out}Z)0(1-X)00$ |
| $\theta_5\ 0Z\rho^5_{out}0101$ | $\theta_5\ 0X(I+p^5_{out}Z)0(1-X)01$ |
| $\theta_6\ 0Z\rho^6_{out}0110$ | $\theta_6\ 0X(I+p^6_{out}Z)0(1-X)10$ |
| $\theta_7\ 0Z\rho^7_{out}0111$ | $\theta_7\ 0X(I+p^7_{out}Z)0(1-X)11$ |
| $\theta_8\ 0Z\rho^8_{out}1000$ | $\theta_8\ 0Z(I+p^8_{out}Z)1(1+X)00$ |
| $\theta_9\ 0Z\rho^9_{out}1001$ | $\theta_9\ 0Z(I+p^9_{out}Z)1(1+X)01$ |
| $\theta_{10}\ 0Z\rho^{10}_{out}1010$ | $\theta_{10}\ 0Z(I+p^{10}_{out}Z)1(1+X)10$ |
| $\theta_{11}\ 0Z\rho^{11}_{out}1011$ | $\theta_{11}\ 0Z(I+p^{11}_{out}Z)1(1+X)11$ |
| $\theta_{12}\ 0Z\rho^{12}_{out}1100$ | $\theta_{12}\ 0X(I+p^{12}_{out}Z)1(1-X)00$ |
| $\theta_{13}\ 0Z\rho^{13}_{out}1101$ | $\theta_{13}\ 0X(I+p^{13}_{out}Z)1(1-X)01$ |
| $\theta_{14}\ 0Z\rho^{14}_{out}1110$ | $\theta_{14}\ 0X(I+p^{14}_{out}Z)1(1-X)10$ |
| $\theta_{15}\ 0Z\rho^{15}_{out}1111$ | $\theta_{15}\ 0X(I+p^{15}_{out}Z)1(1-X)11$ |

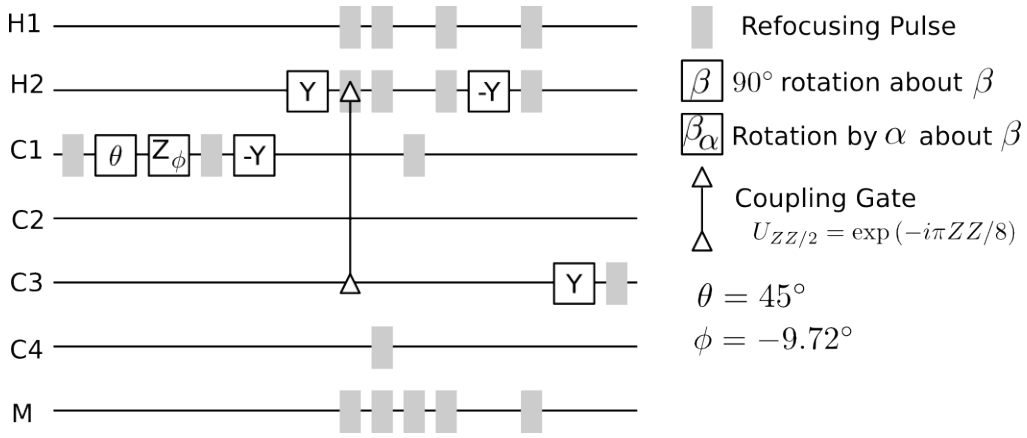


Figure 6.16: Measurement pulse sequence

However, despite their high simulated fidelities the depolarization pulses, especially the RF and chemical shift robust versions, seem to introduce significant errors into the distillation process. It is possible that the robust pulses, although possessing similar total fidelity to the non-robust versions, do not perform as well on this specific input state. Furthermore, the difference in distillation between the simulations from an ideal pseudo-pure state versus a simulated-from-thermal pseudo-pure state indicate that small errors in the initial state preparation significantly affect the distillation. It may be possible to use a phase cycled pseudo-pure state and higher fidelity depolarization pulses to reduce the errors in state preparation.

## 6.8 Probability Measurement

As mentioned previously, the magic state distillation is a probabilistic algorithm, meaning that successful distillation occurs only some fraction of the time. However, if the amount of achieved distillation is known it is possible to compare the predicted probability of success to the experimental probability of success. As stated before, if the distillation sequence is followed by two rotations on $C_1$ the state can be transformed to include the observable $\theta_0 p_{out} 0ZX0000$. By fitting the spectrum it is possible to determine what fraction

Table 6.4: State to State Fidelities for Initial State Preparation

| **Sequence** | $\mathbf{F}_{ideal}$ |
|---|---|
| Polarization crush | .9965 |
| Methyl spin-$\frac{1}{2}$ selection | - [1] |
| Pseudo-pure preparation | .9847 |
| Depolarization | .9981[2] |
| T-rotation | .9977[2] |

[1] Accurate information unavailable due to simulation software limitations.

[2] Average values for the different depolarization amounts.

of observable terms are in the state $\theta_0 p_{out} 0ZX0000$. As $p_{out}$ is now known, it is possible to calculate $\theta_0$. See Figure 6.18 for the extracted $\theta_0$ values.

## 6.9 Sequence Fidelity

Due to the errors introduced in the distillation process by imperfect input states, each section of the state preparation algorithm was simulated independently using an ideal input state to determine where the errors arose. The output of each stage was compared to the ideal output. The measure used for comparison is the normalized trace fidelity given by

$$F(\rho_1\rho_2) = \frac{tr(\rho_1\rho_2)}{\sqrt{tr(\rho_1^2)tr(\rho_2^2)}}. \tag{6.8}$$

The normalizing factor (denominator) was included so that the fidelity would be appropriately scaled even if the total amount of signal decreased, such as through the use of a crusher gradient. The results of the simulations are presented in Table 6.4. The simulated fidelities indicate a general high level of control over the quantum system, although there is the most room for improvement in the pseudo-pure state preparation.

Table 6.5: State Preparation $T_2$ Loss

| **Sequence** | **Duration (ms)** | $T_2$ **Loss** |
|---|---|---|
| Crush | 3 | .9999 |
| M 1/2 Selection | 13 | .9773 |
| Pseudo-Pure Encoding | 33 | .9311 |
| Pseudo-Pure Decoding | 37 | .8099 |
| Total | 86 | .7369 |

## 6.10 $T_2$ Simulation

The amount of signal loss due to transverse relaxation processes was calculated for the pseudo-pure state preparation and distillation sequences. The simulation tracks the coherences at each time step and calculates the amount of signal loss (decoherence) for each coherence according to

$$\rho_{coherence} \longrightarrow e^{-\sum_i \frac{t}{T_2^i}} \rho_{coherence} \tag{6.9}$$

where the sum is over all spins in the xy-plane for that coherence, and $T_2^i$ is the $T_2$ for the $i^{th}$ spin. For simplicity, the $T_2$ loss is only calculated for time between pulses, not during them. The simulation indicates approximately how much signal loss can be attributed to decoherence versus errors in the sequence or implementation. Worst case $T_2$ values, based on the spectra line widths, were used in order to place an upper bound on the amount of signal loss due to relaxation processes. These simulations indicate that at most 26% of the desired signal is lost in the pseudo-pure state preparation due to decoherence. See Table 6.5.

As the amount of achieved distillation is extracted by the ratio of two observables, it is critical that these observables decohere at similar rates. If one term relaxes significantly faster than the other, the distillation values will be incorrect. Simulations indicate that relaxation affects the $0ZZ0X11$ observable significantly more than the $0ZI0X11$ observable. This implies that $T_2$ relaxation processes will prevent the proposed experimental distillation of a magic state, unless the effective experimental $T_2$ is longer than some threshold. This

threshold is approximated by simulating the distillation process with varying $T_2$ values. To isolate the relaxation effects these simulations were conducted with ideal $|T^{enc}\rangle\langle T^{enc}|$ input states. As shown in Figure 6.19, $T_2$ times less than 1 s prevent distillation.

## 6.11 Distillation Robustness Simulations

Due to the imperfect nature of experimental work it is important to determine the robustness of the distillation procedure to variations in $\rho_{in}$. In this simulation the five input states are replaced by

$$\rho_{in} = \frac{1}{2}\left[I + \frac{1}{\sqrt{3}}\left((p^i + \delta_x^i)X + (p^i + \delta_y^i)Y + (p^i + \delta_z^i)Z\right)\right] \tag{6.10}$$

where $\delta_j^i$ are chosen independently from a Gaussian distribution for each spin. In this scheme faulty input states are independently perturbed off of the T-direction. The simulation shows that for reasonable distributions of $\rho_{in}$ the distillation process will succeed. See Figure 6.20. These results seem to indicate that the prepared states in Section 6.5.5 should be distillable, which to a certain degree contradicts the results of Section 6.7. Therefore this analysis appears to not fully capture the effect of the state preparation errors.

## 6.12 Experimental Feasibility

Based on the simulations in this section several conclusions can be drawn about the feasibility of an experimental NMR implementation of a magic state distillation.

First, it appears that the actual distillation and measurement pulse sequences work correctly provided that a) the $|T^{enc}\rangle\langle T^{enc}|$ input states are created accurately enough and b) the $T_2$ times are sufficiently long.

However, it seems that a sufficiently accurate creation of the $|T^{enc}\rangle\langle T^{enc}|$ input states will be a significant experimental challenge. The current pseudo-pure state preparation and depolarization pulses, despite their high fidelities, appear to create input states that do not produce the expected distillation curves. However, the distilled values are close

enough to the distillation curve to justify the assumption that minor improvements to the input state preparation process will yield a convincingly successful magic state distillation.

Therefore, as no fundamental issues prevent the simulated distillation of a magic state, it becomes necessary to determine if experimental control can match the necessary level of control used in the simulations.

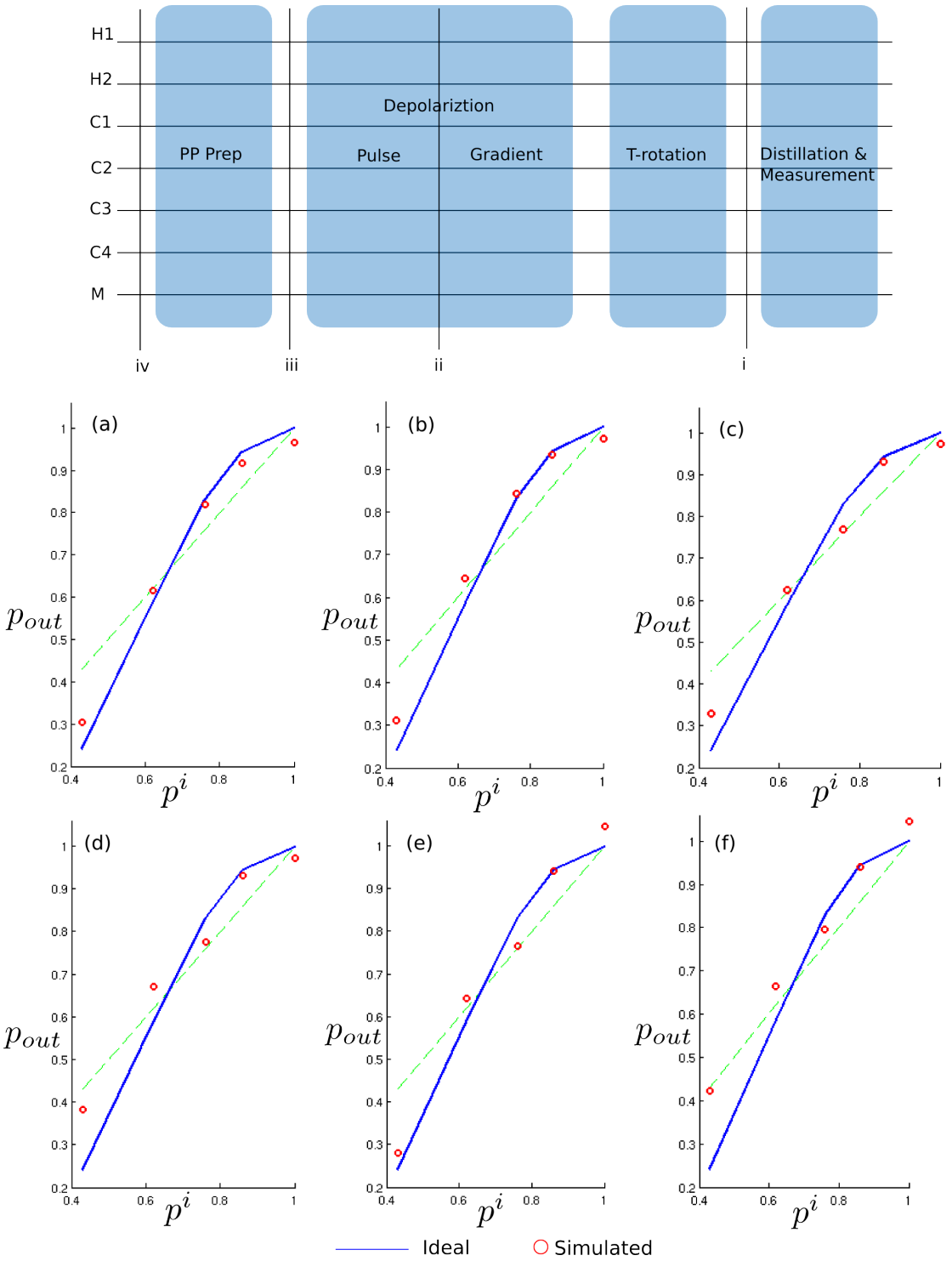


Figure 6.17: Distillation results for simulations with ideal input states starting from (a) i, (b) ii, (c) iii with depolarization pulses that are not robust to RF power and chemical shift variations, (d) iii with robust depolarization pulses, (e) iv with non-robust pulses, and (f) iv with robust pulses.

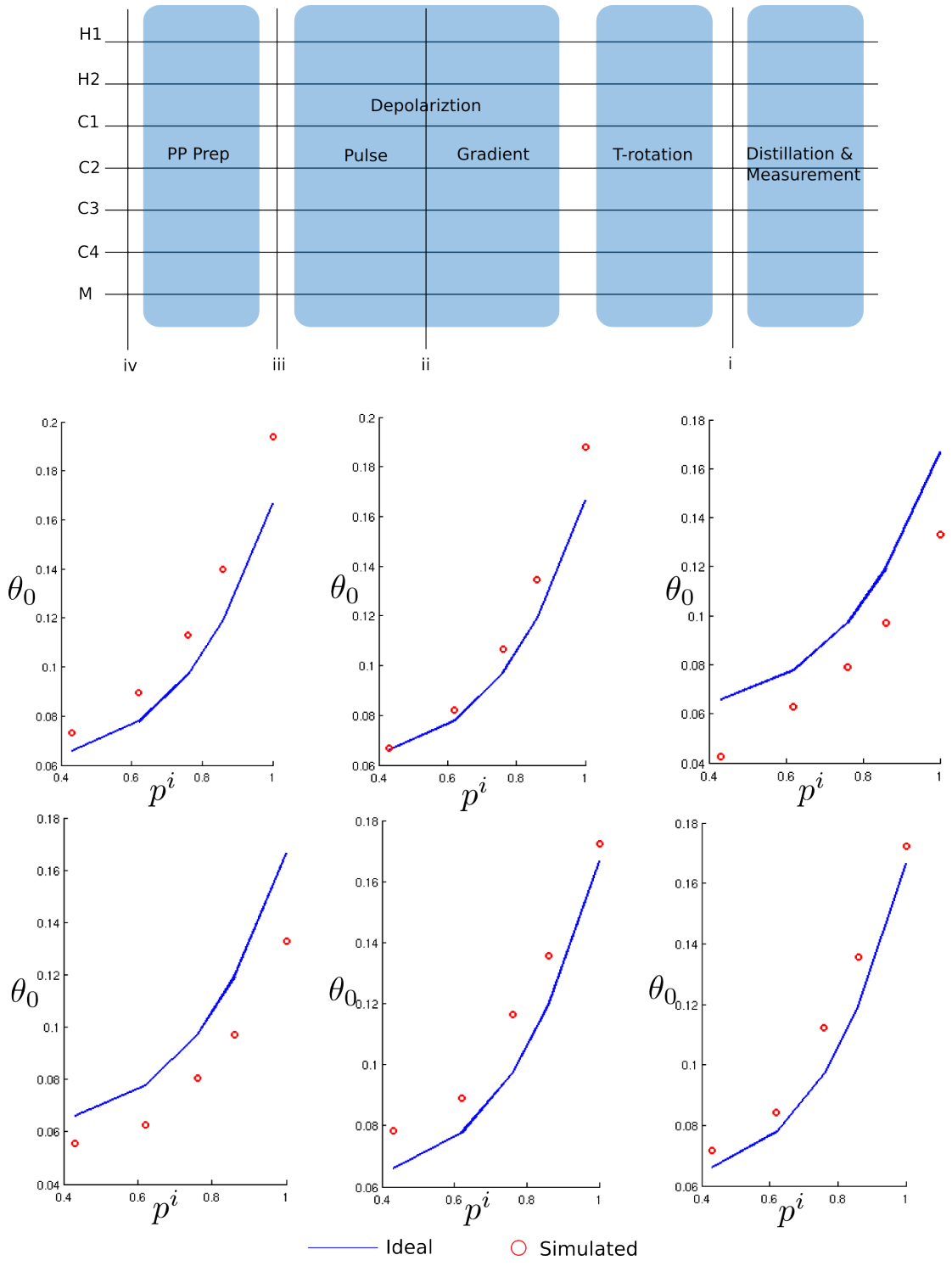


Figure 6.18: Probability of successful distillation for simulations with ideal input states starting from (a) i, (b) ii, (c) iii with depolarization pulses that are not robust to RF power and chemical shift variations, (d) iii with robust depolarization pulses, (e) iv with non-robust pulses, and (f) iv with robust pulses.

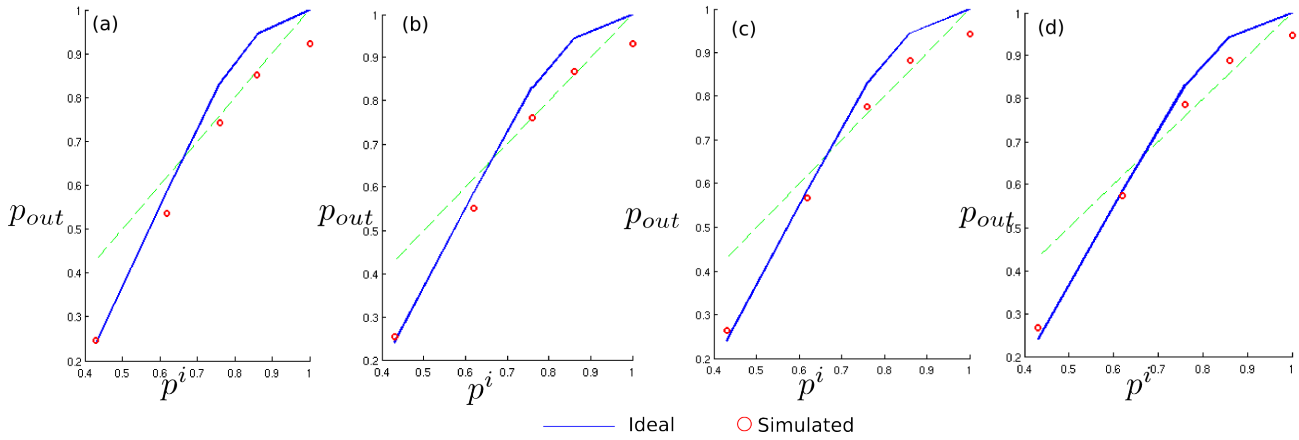


Figure 6.19: Distillation curves for $T_2$ times of (a) .75 s (b) 1 s (c) 1.5 s and (d) 2 s. These results indicate that decoherence times of greater than 1 s are required for successful distillation

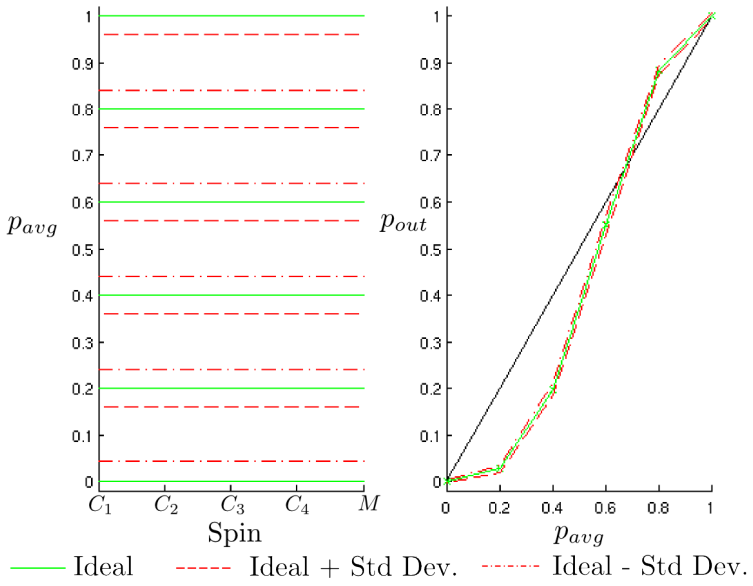


Figure 6.20: Simulation results for the Gaussian distribution of faulty input states as described in Section 6.11. Note that successful distillation is still possible for a reasonable distribution of initial depolarization amounts.

# Chapter 7

# Experiment

The following are results from a preliminary experimental implementation of the magic state distillation algorithm. The goal of this preliminary work is to determine whether sufficient experimental control exists for the magic state distillation, and if not, what challenges must be overcome to attain that control. For this work signal intensities are compared using the relavent peak integrals. Unless otherwise noted, there is an uncertainty of the least significant digit of $\pm 1$.

## 7.1 System Characterization

### 7.1.1 Hamiltonian

The first step to an experimental implementation of the magic state distillation is to accurately characterize the system's properties. First, the system specific Hamiltonian is determined. This is accomplished by a series of experiments that, starting from the thermal state, create states of the form $XIIIIII$ for each spin. Fitting software is used to extract the chemical shift and coupling values. Although fitting the reference spectra provided the magnitude of the J-couplings, the signs of the couplings were gathered from previous work [13]. The chemical shift and J-coupling values are listed in Figure 6.2.

### 7.1.2 Relaxation Parameters

Relaxation, which results in the loss of quantum information, affects the system in two ways. The first, longitudinal relaxation, is the method by which the system returns to thermal equilibrium. The effect of longitudinal relaxation can be modelled as

$$\rho \longrightarrow (\rho - \rho_{EQ})e^{\frac{-t}{T_1}} + \rho_{EQ}. \tag{7.1}$$

The second, transverse relaxation is the process by which microscopic fluctuations in the magnetic field cause the spins to lose synchrony or coherence. Transverse relaxation can be modelled as in equation 6.9.

For this system longitudinal relaxation times are on the order of seconds and do not limit the pulse sequence durations. However, because each experiment requires that the methyl spins start in thermal equilibrium the methyl $T_1$ dictates the minimum delay between experiments. As each experiment is repeated 50 times (RF selection requires two experiments and each of those is repeated 25 times to boost the signal-to-noise), it is desirable to keep the delay between experiments as short as possible. The longitudinal relaxation constant is determined by an inversion recovery experiment [17]. The experiment consists of a 180° pulse, a delay $\tau$, and a 90° readout pulse. This process is repeated for various $\tau$ and the results fit to

$$S(\tau) \propto 1 - 2e^{\frac{\tau}{T_1}} \tag{7.2}$$

Methyl's $T_1$ is $2.9 \pm .1s$. The delay between experiments is set to approximately $5T_1$, meaning that less than 1% of the signal from the previous experiment will remain following the delay.

A preliminary estimate of the decoherence times, $T_2^*$, is calculated from the peak widths of each spin. See Table 7.1 for a list of the values for each spin. However, this estimate is a worst case scenario as it includes decoherence from macroscopic variations in the magnetic fields, which will be refocused to some degree by the pulse sequence. Previous work with this molecule recorded decoherence times greater than 2 s [13]. However as it is not known to what degree the experimental pulse sequence will refocus macroscopic decoherence, the effective $T_2$ likely lies between these two boundaries. Future work may

Table 7.1: Experimental $T_2^*$ values based on line widths.

| **Spin** | $T_2^* \pm 0.03$**s** |
|---|---|
| $H_1$ | 0.45 |
| $H_2$ | 0.46 |
| $C_1$ | 0.70 |
| $C_2$ | 0.51 |
| $C_3$ | 0.97 |
| $C_4$ | 0.82 |
| $M$ | 0.49 |

involve determining a more accurate effective decoherence time during the pulse sequence. However for preliminary work it is reasonable to assume that $T_2$ effects, although hurting the distillation, will not by themselves prevent it (see section 6.10).

### 7.1.3 Crusher Gradient Time

The minimum duration for a polarization crushing gradient is determined with the following experiment. Starting from a thermal state, $M$ is rotated into the plane, a gradient of 20% total strength is applied for duration $\tau$, followed by observation. Note that due to carbon's smaller gyromagnetic ratio a longer gradient is required to crush carbon signal. However, experimentally the signal-to-noise ratio is significantly higher for hydrogen, allowing a more accurate observation of the remaining signal. A duration of 2 ms is sufficient to crush any detectable signal, if the gradient strength is at least 20%.

## 7.2 Pulse Calibration

Approximate pulse powers are determined by using the pulses to perform 360° rotations of the target spins and adjusting the powers to minimize the observed signal. The pulse powers

are fine tuned by a similar signal minimization after RF selection, polarization elimination on all by methyl, and a polarization transfer to the appropriate spin. This procedure does not apply to the Specialty pulses listed in Table 6.1. However, as the GRAPE pulses are calibrated with respect to each other, calibration of 90° GRAPE hydrogen and carbon pulses yields the power levels for all GRAPE pulses.

## 7.3 Pulse Fixing

Although typically very precise instruments, due to technical limitations the spectrometer may introduce small errors in amplitudes of the x and y components of a pulse. For simple pulse shapes the errors can generally be corrected by adjusting the overall power of the pulse. However, for complex pulse shapes, such as GRAPE shapes, the errors cannot be fixed by an overall power correction.

To solve these problems a feedback system is used. During this process a sample containing a pickup coil is inserted in the spectrometer. Using the receiving channel on the spectrometer, the signal detected by the coil is recorded during the application of a pulse. Using this information a program then modifies the pulse such that the output from the spectrometer more closely matches the desired pulse. This process is iterated until a sufficiently accurate pulse implementation is acheived. See Figure 7.1. This process is used on all GRAPE pulses and the RF selection pulses, which were being slightly ramped from start to finish.

## 7.4 RF Selection

The RF selection sequence is evaluated in two ways; how much signal is retained after RF selection and how much 'better behaved' is the remaining signal. By comparing the amount of signal from a thermal methyl spectrum to the amount of signal after the RF selection pulse is applied, indicates that only 33% of the signal is retained when performing RF selection.

The improvement in the behavior of the retained signal is determined by comparing

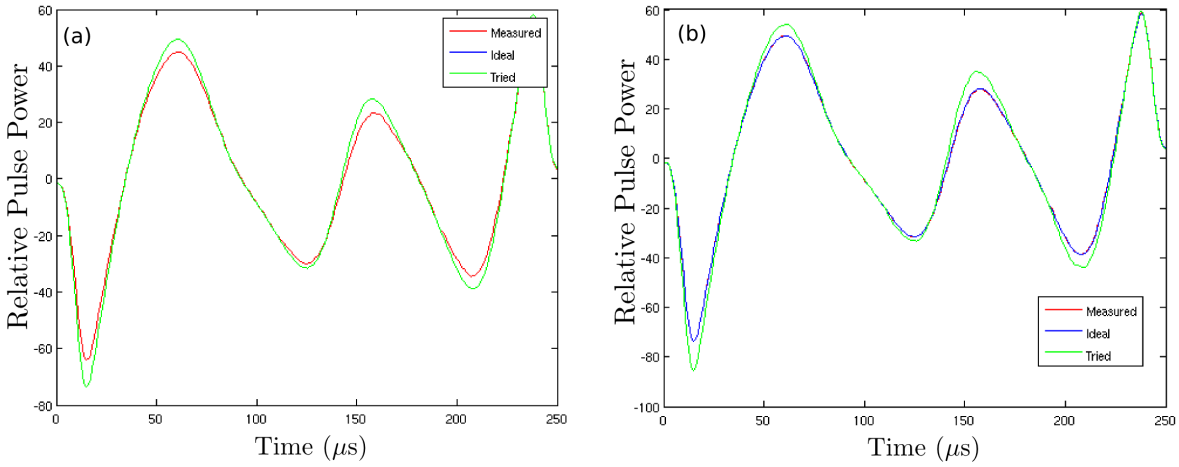


Figure 7.1: Plots of relative pulse power versus time for the MCall5 pulse before and after pulse fixing. 'Measured' corresponds to the amplitude recorded by the feedback coil. 'Ideal' is the desired output and 'Tried' is the RF amplitude that the spectrometer is attempting to implement. (a) Pulse amplitude before pulse fixing. Note that the 'ideal' plot is hidden by the 'tried' plot. (b) Pulse Amplitude after pulse fixing. Note that 'Measured' plot is now hidden by the 'ideal' plot.

the amount of signal before and after performing six 180° pulses with and without RF selection. In the experiment without RF selection, only 63% of the hydrogen signal is retained while when RF selection is used greater than 99% of the RF selected signal is left. Note that when the RF selected signal is transferred to $C_1$, after performing the same experiment, greater than 98% of the signal is retained. This indicates that RF selection on the carbon channel is likely not necessary.

## 7.5 Crusher Sequence

The effectiveness of the crusher sequence is tested by looking at the amount of signal remaining on each spin after performing the crusher sequence. The methyl retained 98.8%

of its signal while the others retained on average about 6%. Repetition of the process did not significantly decrease the detectable polarization of the carbon spins indicating that the problem was likely not a simple power miscalibration. Further investigation into the source of this remaining polarization is necessary.

## 7.6 M-$\frac{1}{2}$ Selection

The M-$\frac{1}{2}$ selection sequence is tested by observing $C_1$ before and after the sequence. See Figure 7.2 for the spectra. The outer peaks decrease from 33% to 3% of the inner peaks. Ideally the outer peaks should be completely removed.

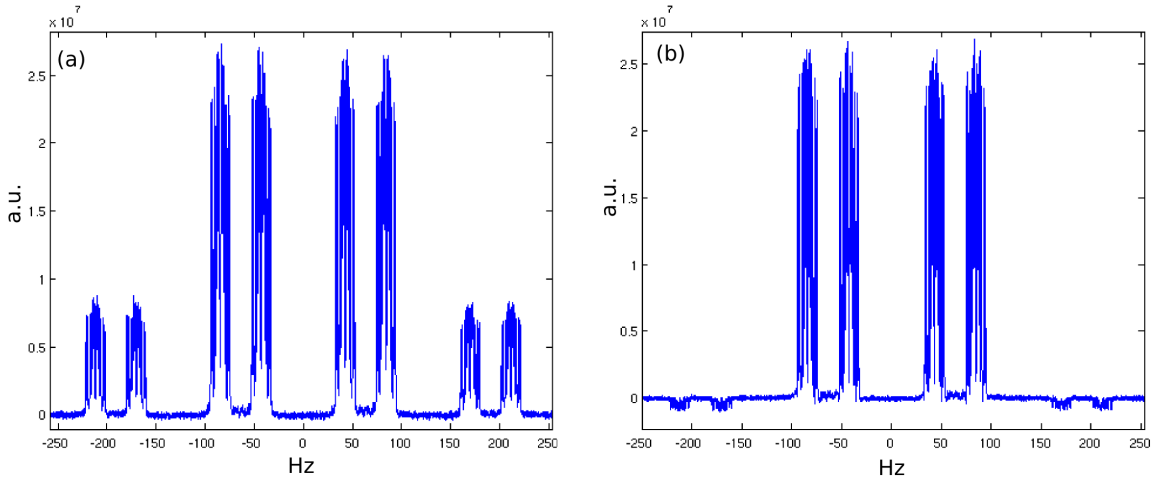


Figure 7.2: Experimental carbon spectrum (a) before and (b) after methyl spin-$\frac{1}{2}$ selection. Note that the outer peaks are not completely eliminated indicating control imperfections.

## 7.7 Pseudo-Pure State Preparation

The pseudo-pure state is observed after rotating $H_2$ into the plane. The amount of signal lost, compared to an ideal preparation, is determined by comparing the peak integrals

from a reference spectrum (methyl polarization transferred to $H_2$) to the pseudo-pure peak integral. After accounting for signal loss in the reference polarization transfer, the pseudo-pure peak has an intensity of $47 \pm 1\%$ of an ideal preparation. The amount of signal loss is significantly more than is expected from relaxation processes alone.

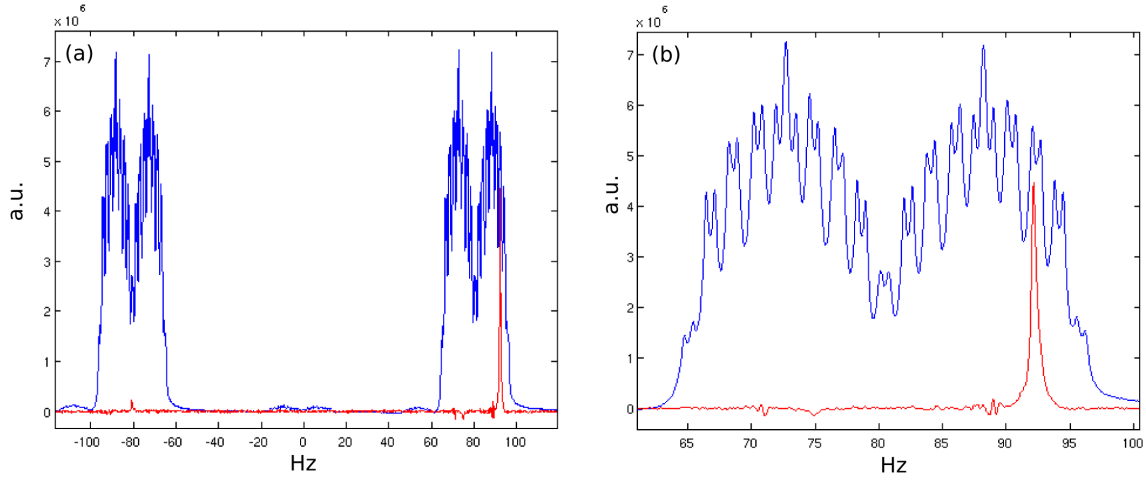


Figure 7.3: Experimental $H_2$ pseudo-pure and thermal reference spectra. (a) Entire $H_2$ spectra and (b) zoomed spectra.

## 7.8 Depolarization and T-Rotation

The depolarization and T-rotation pulses are first tested on the thermal state by comparing a reference spectrum to the spectrum generated by a depolarization pulse. From these values the amount of signal remaining along the z-axis is calculated. See Tables 7.2 and 7.3.

As mentioned in the NMR implementation section, the depolarization is also measured after the depolarizing sequence and a readout pulse on $C_1$. The five spectra of $C_1$ are shown below for depolarization amounts corresponding to $p^i = 1, 0.86, 0.76, 0.62, 0.43$. These spectra are fit and the $p^i$ values are plotted in Figure 7.4. The difference in depolarization

Table 7.2: Depolarization amounts - Signal in the plane.

| **Spin** | **MCall2** | **MCall3** | **MCall4** | **MCall5** | **Trot** |
|---|---|---|---|---|---|
| **Ideal** | .51 | .65 | .78 | .90 | .82 |
| $C_1$ | .47 | .62 | .79 | .90 | .81 |
| $C_2$ | .50 | .64 | .81 | .93 | .83 |
| $C_3$ | .50 | .63 | .77 | .90 | .81 |
| $C_4$ | .51 | .61 | .75 | .84 | .77 |
| $M$ | .50 | .61 | .73 | .86 | .79 |

Table 7.3: Depolarization amounts - Signal along the z-axis.

| **Spin** | **MCall2** | **MCall3** | **MCall4** | **MCall5** | **Trot** |
|---|---|---|---|---|---|
| **Ideal** | .86 | .76 | .62 | .43 | .58 |
| $C_1$ | .88 | .78 | .62 | .44 | .59 |
| $C_2$ | .87 | .77 | .59 | .37 | .56 |
| $C_3$ | .87 | .78 | .64 | .44 | .58 |
| $C_4$ | .86 | .79 | .66 | .54 | .63 |
| $M$ | .87 | .80 | .69 | .51 | .61 |
| **Avg** | .87 | .78 | .64 | .46 | .60 |
| **STD** | .01 | .01 | .04 | .07 | .03 |

values extracted from this process and those expected from the tests of the depolarization pulses on the thermal state indicate that either the state preparation process is introducing significant errors or the fitting and extraction process is not working accurately.

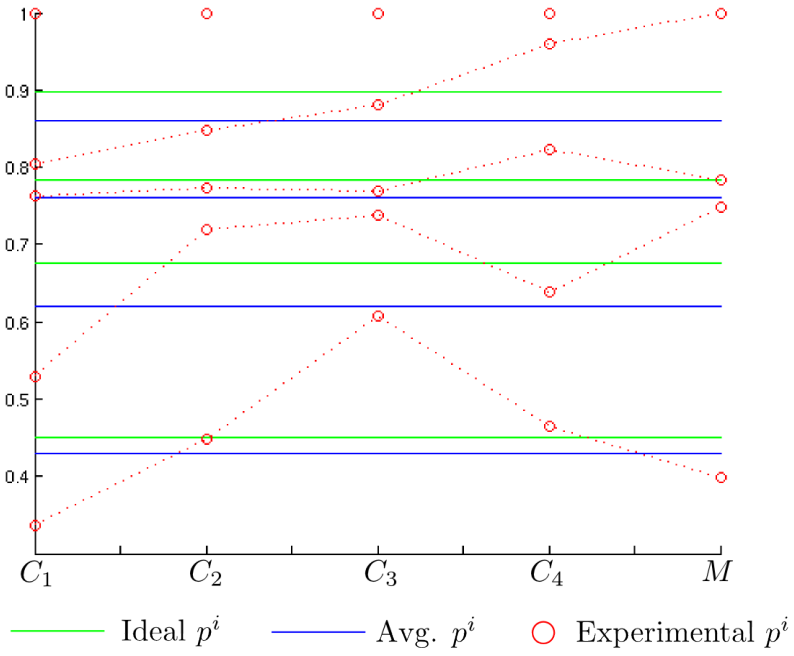


Figure 7.4: Experimental depolarization amounts as extracted according to Section 6.5.5 from the spectra in Figure 7.5.

## 7.9 Distillation Measurement

The distillation measurement is implemented as described in section 6.7. Using fitting software the observables are extracted from the $C_3$ spectra in Figure 7.7 and the extracted distillation curve is plotted in Figure 7.6. Although the experiments for smaller $p^i$ appear to follow the distillation curve, the unexpected behavior for the larger $p^i$ values indicates that either the fitting and extraction is not working correctly or that the distillation failed.

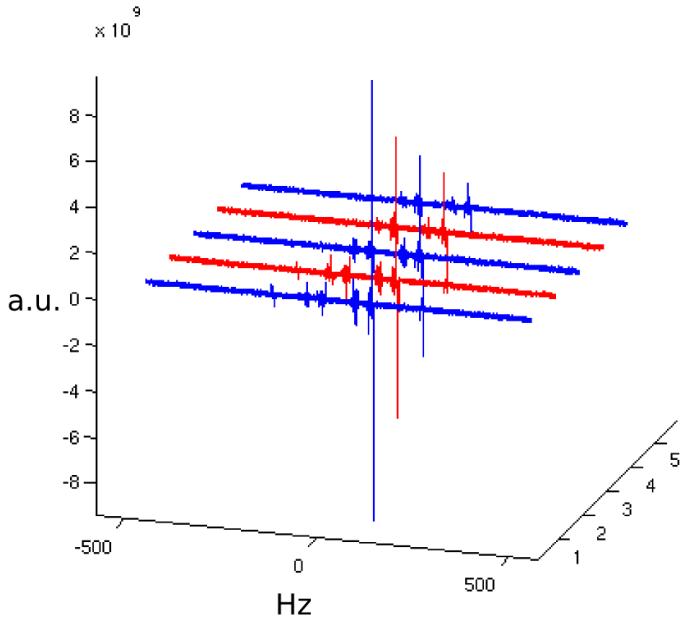


Figure 7.5: Experimental depolarization spectra. Note that the complex spectra and error terms (as described in Section 6.5.5) make the fitting and extraction of observables difficult.

## 7.10 Probability Measurement

Following the procedure in section 6.8, $C_1$ is observed after the distillation sequence and the probability of successful distillation is extracted from the data.

## 7.11 Analysis of Experimental Control

Although the above results are preliminary, it appears that there are no fundamental issues preventing successful distillation. However, improvements must be made before experimental control matches the level of control used in the simulations. This is especially evident in the state preparation stage where excessive signal loss and error terms indicate

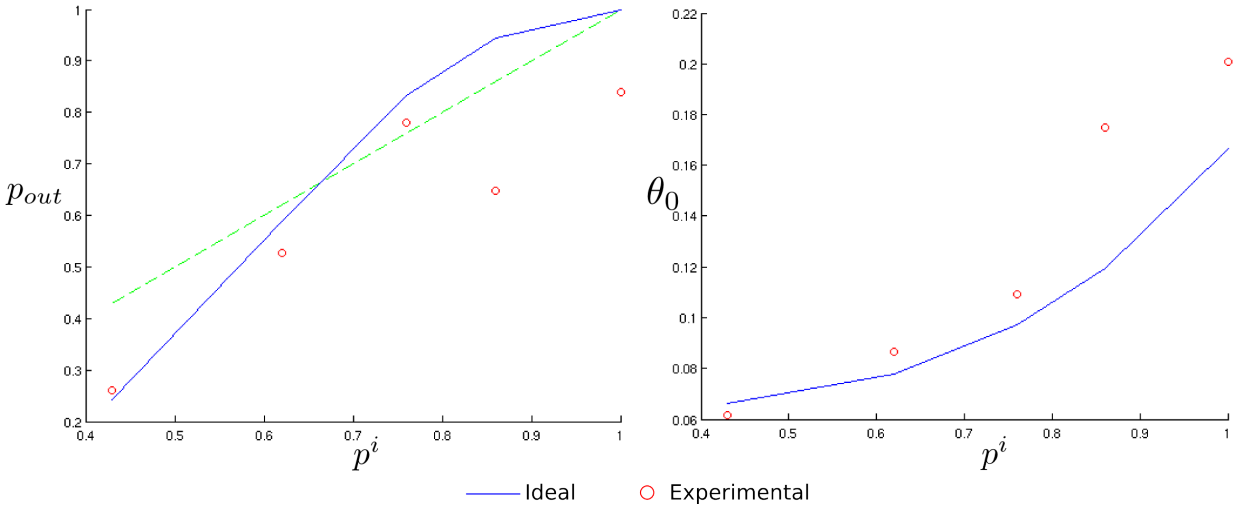


Figure 7.6: Experimental distillation and probability of success curves. States with smaller $p^i$'s appear to be correctly distilled while states with larger initial polarizations are not distilled.

a level of control below that used in the simulations. Finally, the unexpected deviations from the distillation curve for small depolarizations indicates that improvements may need to be made in the fitting and extraction of observables.

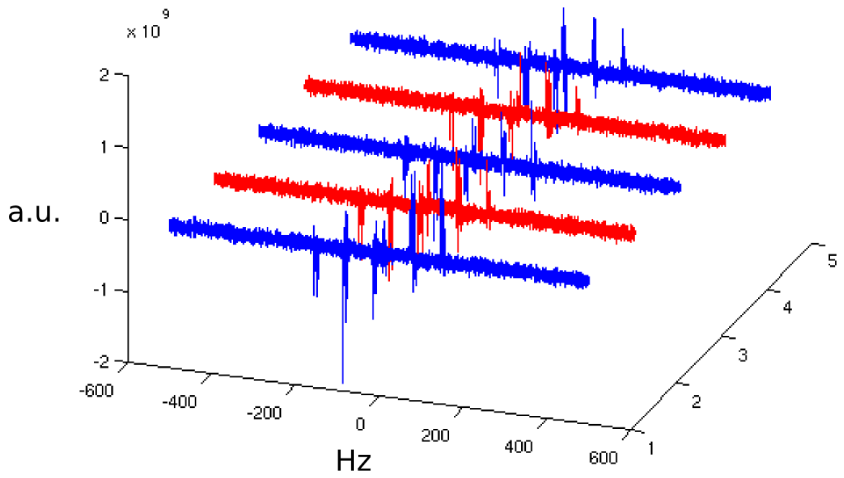


Figure 7.7: Experimental distillation - $C_3$ spectra. These spectra are used as outlined in Section 6.7 to calulate the amount of distillation achieved. Note that the complex spectra, error terms, and a low signal-to-noise ratio make the analysis difficult.

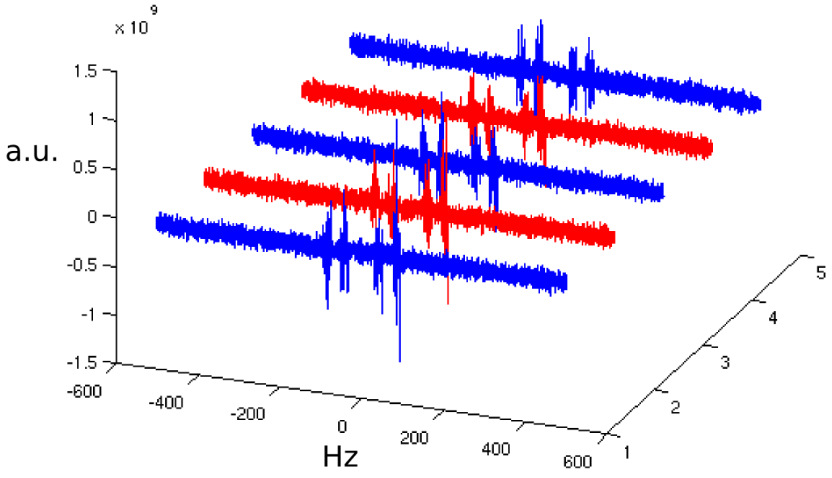


Figure 7.8: Experimental distillation - $C_1$ spectra. These spectra are used as outlined in Section 6.8 to calulate the probability of successful distillation. Note that the complex spectra, error terms, and a low signal-to-noise ratio make the analysis difficult.

# Chapter 8

# Conclusions

Magic state distillation is an essential component in the fault tolerant computational model proposed by Bravyi and Kitaev. As this model promises a relatively high error rate threshold, the successful distillation of a magic state would be a significant step towards experimental fault tolerant QIP.

The goal of this work was to determine if an NMR implementation of the magic state distillation is feasible with the current level of control, and if so, to perform an experimental demonstration of the magic state distillation.

This work demonstrated that it is theoretically possible to distill magic states using NMR. However, simulations indicated that a very high level of control must be attained for such a distillation to succeed. This is especially relevant in the preparation of the faulty input states. Simulations also indicated that decoherence effects dramatically reduce that amount of distillation possible, further emphasizing the need for precise control.

Each stage of the procedure was experimentally implemented and analyzed. These results illustrated that although there are no fundamental limitations, the implementation requires a high level of experimental control that was not present in preliminary experiments. Furthermore, unexpected variations in the extracted distillation values indicated that the extraction process may be introducing errors.

Future work will involve improving the initial state preparation through the use of higher fidelity depolarization pulses, phase cycling, and better sequence optimization.

Work will also focus on determining the effective decoherence times, optimizing experimental control, and improving the accuracy and reliability of the observable extraction process.

# Bibliography


[1] J. Baugh, J. Chamilliard, C. M. Chandrashekar, M. Ditty, A. Hubbard, R. Laflamme, M. Laforest, D. Maslov, O. Moussa, C. Negrevergne, M. Silva, S. Simmons, C. A. Ryan, D. G. Cory, J. S. Hodges, and C. Ramanathan. Quantum information processing using nuclear and electron magnetic resonance: review and prospects. arXiv:quant-ph/07101447, 2007.

[2] J. Baugh, O. Moussa, C. A. Ryan, A. Nayak, and R. Laflamme. Experimental implementation of heat-bath algorithmic cooling using solid-state nuclear magnetic resonance. *Nature*, 438(7067):470–473, 2005.

[3] C. H. Bennett, D. P. DiVincenzo, J. A. Smolin, and W. K. Wootters. Mixed-state entanglement and quantum error correction. *Physical Review A*, 54(5):3824–3851, 1996.

[4] P. O. Boykin, T. Mor, V. Roychowdhury, F. Vatan, and R. Vrijen. Algorithmic cooling and scalable nmr quantum computers. *Proceedings of the National Academy of Sciences of the USA*, 99:3388–3393, 2002.

[5] S. Bravyi and A. Kitaev. Universal quantum computation with ideal clifford gates and noisy ancillas. *Physical Review A*, 71(2):022316, 2005.

[6] E. Dennis, A. Kitaev, A. Landahl, and J. Preskill. Topological quantum memory. *Journal of Mathematical Physics*, 43(9):4452–4505, 2002.

[7] D. P. DiVincenzo. The physical implementation of quantum computation. *Fortschritte der Physik*, 48:771–1783, 2000.

[8] R. Feynman. Simulating physics with computers. *International Journal of Theoretical Physics*, 21:467–488, 1982.

[9] E. M. Fortunato, M. A. Pravia, N. Boulant, G. Teklemariam, T. F. Havel, and D. G. Cory. Design of strongly modulating pulses to implement precise effective hamiltonians for quantum information processing. *The Journal of Chemical Physics*, 116(17):7599–7606, 2002.

[10] R. Freeman. Shaped radiofrequency pulses in high resolution nmr. *Progress in Nuclear Magnetic Resonance Spectroscopy*, 32:59–196, 1998.

[11] D. Gottesman. *Stabilizer Codes and Quantum Error Correction*. PhD thesis, Caltech, 1997.

[12] N. Khaneja, T. Reiss, C. Kehlet, T. Schulte-Herbrugger, and S. Glaser. Optimal control of coupled spin dynamics: design of nmr pulse sequences by gradient ascent algorithms. *Journal of Magnetic Resonance*, 172:296–305, 2005.

[13] E. Knill, R. Laflamme, R. Martinez, and C.-H. Tseng. An algorithmic benchmark for quantum information processing. *Nature*, 404(6776):368–370, 2000.

[14] E. Knill, R. Laflamme, and W. H. Zurek. Resilient Quantum Computation. *Science*, 279(5349):342–345, 1998.

[15] R. Laflamme, E. Knill, D. G. Cory, and E. M. Fortunado. Introduction to nmr quantum information processing. arXiv:quant-ph/0207172v1.

[16] R. Laflamme, C. Miquel, J. P. Paz, and W. H. Zurek. Perfect quantum error correcting code. *Physical Review Letters*, 77(1):198–201, 1996.

[17] M. H. Levitt. *Spin Dynamics*. Wiley, West Sussex, England, 2001.

[18] M. A. Nielsen and I. L. Chuang. *Quantum Computation and Quantum Information*. Cambridge University Press, 2004.

[19] C. A. Ryan, O. Moussa, J. Baugh, and R. Laflamme. A spin based heat engine: multiple rounds of algorithmic cooling. arXive e-print quant-ph/0706.2853, 2007.

[20] P. W. Shor. Polynomial-time algorithms for prime factorization and discrete logarithms on a quantum computer. *SIAM Journal on Computing*, 26(5):1484–1509, 1997.

[21] D. R. Simon. On the power of quantum computation. *SIAM Journal on Computing*, 26(5):1474–1483, 1997.

[22] A. M. Steane. Active stabilization, quantum computation, and quantum state synthesis. *Physical Review Letters*, 78(11):2252–2255, 1997.

[23] L. M. K. Vandersypen and I. L. Chuang. Nmr techniques for quantum control and computation. *Reviews of Modern Physics*, 76(4):1037, 2004.